Symmetry Breaking and Ascending in the Magnetic Kagome Metal FeGe

Shangfei Wu,[1,*,†] Mason L. Klemm,[2,*] Jay Shah,[3] Ethan T. Ritz,[3] Chunruo Duan,[2] Xiaokun Teng,[2] Bin Gao,[2] Feng Ye,[4] Masaaki Matsuda,[4] Fankang Li,[5] Xianghan Xu,[1] Ming Yi,[2] Turan Birol,[3,‡] Pengcheng Dai,[2,§] and Girsh Blumberg[1,6,‖]

[1]*Department of Physics and Astronomy, Rutgers University, Piscataway, New Jersey 08854, USA*
[2]*Department of Physics and Astronomy, Rice University, Houston, Texas 77005, USA*
[3]*Department of Chemical Engineering and Materials Science, University of Minnesota, Minnesota 55455, USA*
[4]*Neutron Scattering Division, Oak Ridge National Laboratory, Oak Ridge, Tennessee 37831, USA*
[5]*Neutron Technologies Division, Oak Ridge National Laboratory, Oak Ridge, Tennessee 37831, USA*
[6]*National Institute of Chemical Physics and Biophysics, 12618 Tallinn, Estonia*

(Received 15 September 2023; accepted 24 January 2024; published 8 March 2024)

Spontaneous symmetry breaking—the phenomenon in which an infinitesimal perturbation can cause the system to break the underlying symmetry—is a cornerstone concept in the understanding of interacting solid-state systems. In a typical series of temperature-driven phase transitions, higher-temperature phases are more symmetric due to the stabilizing effect of entropy that becomes dominant as the temperature is increased. However, the opposite is rare but possible when there are multiple degrees of freedom in the system. Here, we present such an example of a symmetry-ascending phenomenon upon cooling in a magnetic kagome metal FeGe by utilizing neutron Larmor diffraction and Raman spectroscopy. FeGe has a kagome lattice structure with simple A-type antiferromagnetic order below Néel temperature $T_N \approx 400$ K and a charge density wave (CDW) transition at $T_{\mathrm{CDW}} \approx 110$ K, followed by a spin-canting transition at around 60 K. In the paramagnetic state at 460 K, we confirm that the crystal structure is indeed a hexagonal kagome lattice. On cooling to around T_N, the crystal structure changes from hexagonal to monoclinic with in-plane lattice distortions on the order of 10^{-4} and the associated splitting of the double-degenerate phonon mode of the pristine kagome lattice. Upon further cooling to T_{CDW}, the kagome lattice shows a small negative thermal expansion, and the crystal structure gradually becomes more symmetric upon further cooling. A tendency of increasing the crystalline symmetry upon cooling is unusual; it originates from an extremely weak structural instability that coexists and competes with the CDW and magnetic orders. These observations are against the expectations for a simple model with a single order parameter and hence can only be explained by a Landau free energy expansion that takes into account multiple lattice, charge, and spin degrees of freedom. Thus, the determination of the crystalline lattice symmetry as well as the unusual spin-lattice coupling is a first step towards understanding the rich electronic and magnetic properties of the system, and it sheds new light on intertwined orders where the lattice degree of freedom is no longer dominant.

DOI: 10.1103/PhysRevX.14.011043 Subject Areas: Condensed Matter Physics

I. INTRODUCTION

Symmetry breaking occurs when a solid changes from one crystalline phase to another at the phase-transition temperature. Landau originally developed a theory of symmetry restrictions on second-order phase transitions in 1937 [1]. When a crystal structure changes continuously from a highly symmetrical phase to a less symmetrical one, the symmetry group of the low-symmetry phase must be a subgroup of the high-symmetry group [2]. Generally, the more symmetrical phase corresponds to higher temperatures, and the less symmetrical phase to lower temperatures. Thus, the symmetry-breaking phenomena are usually detected upon cooling from high temperatures to

*These authors contributed equally to this work.
†wusf@baqis.ac.cn
Present address: Beijing Academy of Quantum Information Sciences, Beijing 100193, China.
‡tbirol@umn.edu
§pdai@rice.edu
‖girsh@physics.rutgers.edu

low temperatures in different types of phase transitions, including structural, incommensurate, magnetic, and liquid crystal systems [3]. Exceptions of the symmetry breaking, namely, symmetry ascending, from the high-temperature phase to the low-temperature phase in a second-order phase transition are reported in Rochelle salt crystals (monoclinic to orthorhombic) [4] and mixed crystals $Tb_pGd_{1-p}VO_4$ (orthorhombic to tetragonal) [5]. These exceptions typically suggest the importance of additional interactions such as spin-lattice coupling or cooperative Jahn-Teller interactions to the structural phase transition. The symmetry-ascending phenomena are also reported in the first-order-like transitions in iron-based and cuprate superconductors [6–9]. For example, the parent compound of iron pnictide superconductors order antiferromagnetically and ferromagnetically along two Fe-Fe directions of the nearly square lattice to form a stripe antiferromagnetic (AFM) structure [10]. Since the magnetic structure has the twofold rotational (C_2) symmetry, the crystalline lattice must also exhibit a tetragonal-to-orthorhombic (C_4 to C_2) lattice distortion at temperatures at or above the magnetic ordering temperature T_N to accommodate the low-symmetry magnetic structure [10]. However, when the low-temperature magnetic structure becomes C_4 symmetric, as seen in a narrow hole-doped regime of iron pnictides, the lattice symmetry can change from C_2 to C_4 in a first-order-like fashion due to the formation of the C_4 symmetric out-of-plane collinear double-**Q** magnetic ordering [7,8,11,12]. This symmetry ascending upon cooling usually suggests that there are several competing interactions near the phase-transition boundary with similar energy scales [13,14].

The kagome lattice with a corner-shared-triangle network is a fruitful playground to study the exotic electronic orders and symmetry-breaking phenomenon at the interplay between charge, orbital, spin, and lattice degrees of freedom [15,16], including quantum spin liquid, charge density wave (CDW), chiral flux order, nematicity, and superconductivity [17–29]. Signatures of threefold symmetry breaking have been reported in the CDW phase of the related vanadium-based kagome AV_3Sb_5 system by scanning tunneling microscopy (STM), c-axis magnetoresistance, optical, and x-ray measurements [30–34]. Recently, the B35 phase of FeGe with hexagonal kagome lattice structure (P6/mmm, No. 191) [Fig. 1(a)] [35–39] has attracted considerable attention due to the interplay amongst different phases. Below $T_N \approx 400$ K, FeGe orders into a collinear A-type AFM structure. The Fe moments within the same basal plane are coupled ferromagnetically with the spin direction parallel to the c axis, while those in adjacent layers are coupled antiferromagnetically [38]. Below the spin-canting temperature $T_{\text{canting}} = 60$ K, the spins form an AFM double-cone structure with a modulated basal-plane moment while the moments are predominantly pointing along the c axis [38]. At the intermediate temperature, a short-ranged CDW order with a transition temperature $T_{\text{CDW}} \approx 110$ K was discovered by neutron diffraction [39], STM [40], and angle-resolved photoemission spectroscopy (ARPES) measurements [41]. This short-ranged CDW order in FeGe [39] can be further tuned to be long-ranged by postgrowth annealing treatments [42,43]. In particular, CDW order enhances the magnetic-ordered moments, thus establishing a clear coupling between CDW and magnetism [39]. From subsequent x-ray diffraction measurements, the CDW transition is believed to be associated with the c-axis dimerizations of partial Ge^1 atoms in the kagome layer of FeGe [Figs. 1(a) and 1(g)] [42,43], but the crystal structure is still refined to be a hexagonal kagome lattice with the threefold rotational (C_3) symmetry at all temperatures investigated (from 20 K to room temperature) [43,44]. Although density functional theory (DFT) phonon calculations have proposed several possible lattice distortion patterns in the CDW phase [42,45–49], inelastic neutron and x-ray scattering measurements did not detect soft acoustic phonon modes at the Brillouin zone boundary across the CDW transition [41,42].

In this article, we use neutron Larmor diffraction and polarization-resolved Raman spectroscopy to study the temperature-dependent lattice symmetry of FeGe and the associated lattice dynamics. In the paramagnetic state at 460 K, we confirm that the crystal structure is indeed a hexagonal kagome lattice [Figs. 1(a) and 1(d)]. On cooling to below T_N, the C_3 symmetry of the hexagonal kagome lattice is broken, which is revealed by inequivalent in-plane lattice parameters on the order of 10^{-4} and the splitting of a double-degenerate phonon mode [Figs. 1(b), 1(e), and 1(f)]. Upon further cooling to a CDW temperature of $T_{\text{CDW}} \approx 110$ K, the kagome lattice shows a small negative thermal expansion, and the crystal structure gradually becomes more symmetric upon further cooling, resulting in a tendency of lattice symmetry ascending below T_{canting} [Fig. 1(c)]. Since A-type AFM structure is not expected to affect the in-plane kagome lattice structure, our discovery of a series of lattice distortions in the kagome plane, as well as the tendency of lattice symmetry ascending upon cooling, suggests an interplay between magnetic order, CDW, and lattice distortion in FeGe. Our determination of crystalline lattice symmetry forms the basis for understanding the electronic and magnetic properties of the system.

II. RESULTS

A. AFM phase

To precisely determine the temperature evolution of the lattice symmetry of FeGe across T_{N}, we carried out neutron Larmor diffraction measurements, as shown schematically in Fig. 2(a) [50]. Neutron Larmor diffraction is a polarized neutron technique developed to increase the resolution of conventional neutron diffractometers by fully taking advantage of the additional spin degree of freedom of the neutron. Inside an applied magnetic field that guides the spin rotation of the traveling neutrons, the neutron spin will experience a motion called Larmor precession around

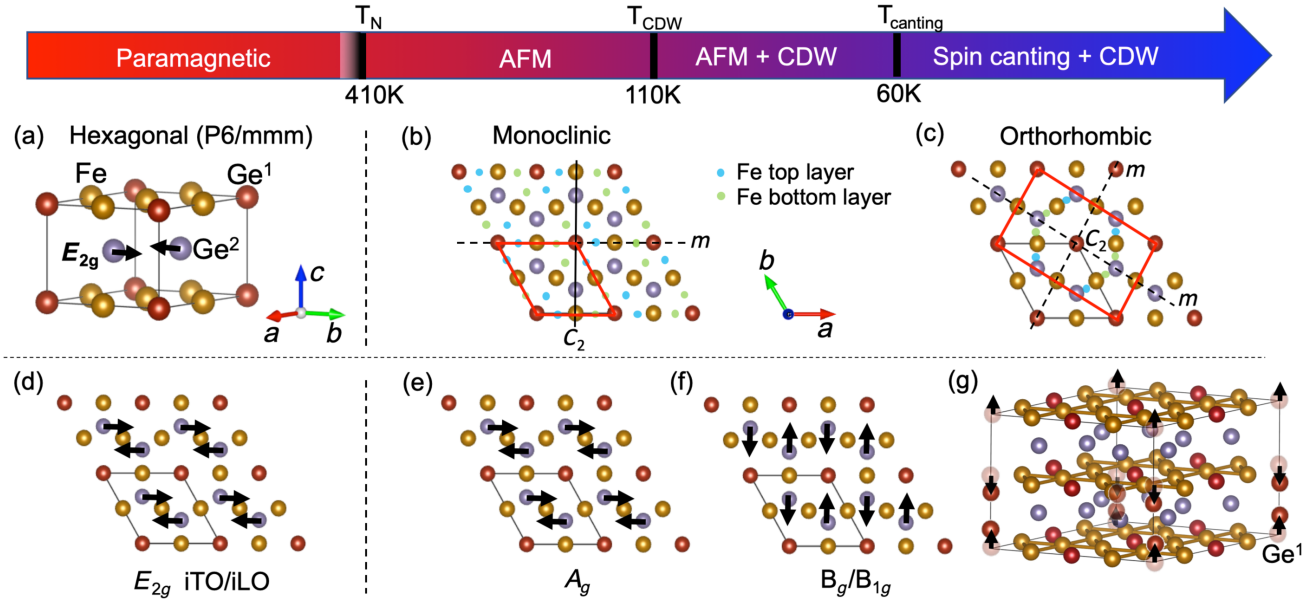

FIG. 1. Crystal structure of FeGe in the nonmagnetic phase ($T > T_N$). The Ge atoms in the kagome and honeycomb layers are marked by Ge^1 and Ge^2, respectively. The black arrows in panel (a) represent the $E_{2g}(Ge^2)$ in-plane lattice vibration pattern. (b) Illustration of the monoclinic AFM unit cell (space group $P2_1/m$) driven by the A_6^- lattice instability shown by the red diamond. The blue and green solid circles represent an example of the distorted Fe atomic positions within the unit cell for the top and bottom layers, respectively. The dashed lines represent the mirror planes. The C_2 axis is perpendicular to the threefold axis of the nonmagnetic phase. (c) Same as panel (b) but for the orthorhombic AFM unit cell (space group Cmcm) driven by the A_6^- lattice instability shown by the red rectangle. The C_2 axis is parallel to the threefold axis of the nonmagnetic phase. (d) Illustration of the E_{2g} lattice vibration patterns for Ge^2 atoms in the honeycomb layers of the hexagonal nonmagnetic phase (top view). This is a twofold-degenerate mode containing an in-plane transverse optical (iTO) mode and an in-plane longitudinal optical (iLO) mode. (e) Illustration of the A_g (A_g) lattice vibration patterns for Ge^2 atoms in the honeycomb layers for the monoclinic (orthorhombic) phases (top view). (f) Same as panel (e) but for the B_g (B_{1g}) lattice vibration patterns of the monoclinic (orthorhombic) phases. The A_g and B_g (B_{1g}) modes originate from the splitting of the $E_{2g}(Ge^2)$ mode of the nonmagnetic phase shown in panel (d). The back arrows in panels (d)–(f) indicate the vibration directions. (g) Illustration of the crystal structure of the $2 \times 2 \times 2$ CDW phase associated with the c-axis dimerization of partial Ge^1 atoms in the kagome layer of FeGe based on Refs. [42,43]. The black arrows in panel (g) represent the Ge^1 displacement directions.

the magnetic-field vectors. The resulting accumulated Larmor phase Φ is proportional to the magnetic-field intensity B, neutron wavelength λ, and the path length through the magnets L. By tilting the field boundaries of the magnets parallel to the crystal plane of interest before and after the sample, the measurement of the lattice spacing d can be linearly translated into the measurement of the Larmor phase as $\Phi = BLd$. The value of Φ is independent of the beam divergence and the mosaic spread of the sample. For the Larmor diffraction setup at HB-1, magnetic Wollaston prisms [51] are utilized such that the physical tilting of the magnetic-field boundaries can be effectively achieved by picking the appropriate combination of the electromagnetic fields shown in Fig. 2(a), i.e., B and b. The Larmor phase of the neutron spin is observed by a polarization analyzer to yield $P = \cos(\Phi)$. An example of the measured intensity on the detector has been given in Figs. 2(b) and 2(c) for two different values of the lattice constant. By measuring the relative phase shift between the two intensity oscillations with a high precision ($\Delta\Phi/\Phi \sim 10^{-6}$), the same resolution is achieved in measuring the change in the lattice constant $\Delta d/d = \Delta\Phi/\Phi$ for FeGe at the three different Bragg peak positions shown in Fig. 2(d). The temperature dependence of the absolute lattice spacing can be deduced from the measured $\Delta d/d$ for FeGe shown in Figs. 2(e) and 2(f).

In Fig. 2(g), we show the absolute lattice spacing derived from the three different Bragg peak positions (2, 0, 0), (0, 2, 0), and $(2, -2, 0)$. Above 430 K, the temperature dependence of the three lattice spacings is identical. This finding is consistent with an ideal kagome lattice with threefold lattice rotational symmetry. Below T_N, the temperature dependence of the lattice spacing along the (2, 0, 0), (0, 2, 0), and $(2, -2, 0)$ directions deviates, indicating threefold symmetry breaking. The clear three lattice spacing below T_N indicates that the AFM phase is monoclinic (Appendix C). It also suggests that the sample is in a single domain. As discussed in Refs. [50,52], neutron Larmor diffraction can measure the broadening of the Bragg peaks due to lattice distortion formation of twinned domains [see Fig. 1(c) of Ref. [52] and Fig. 4 of Ref. [50]]. In the case of NaFeAs (Ref. [52]), the samples are twinned,

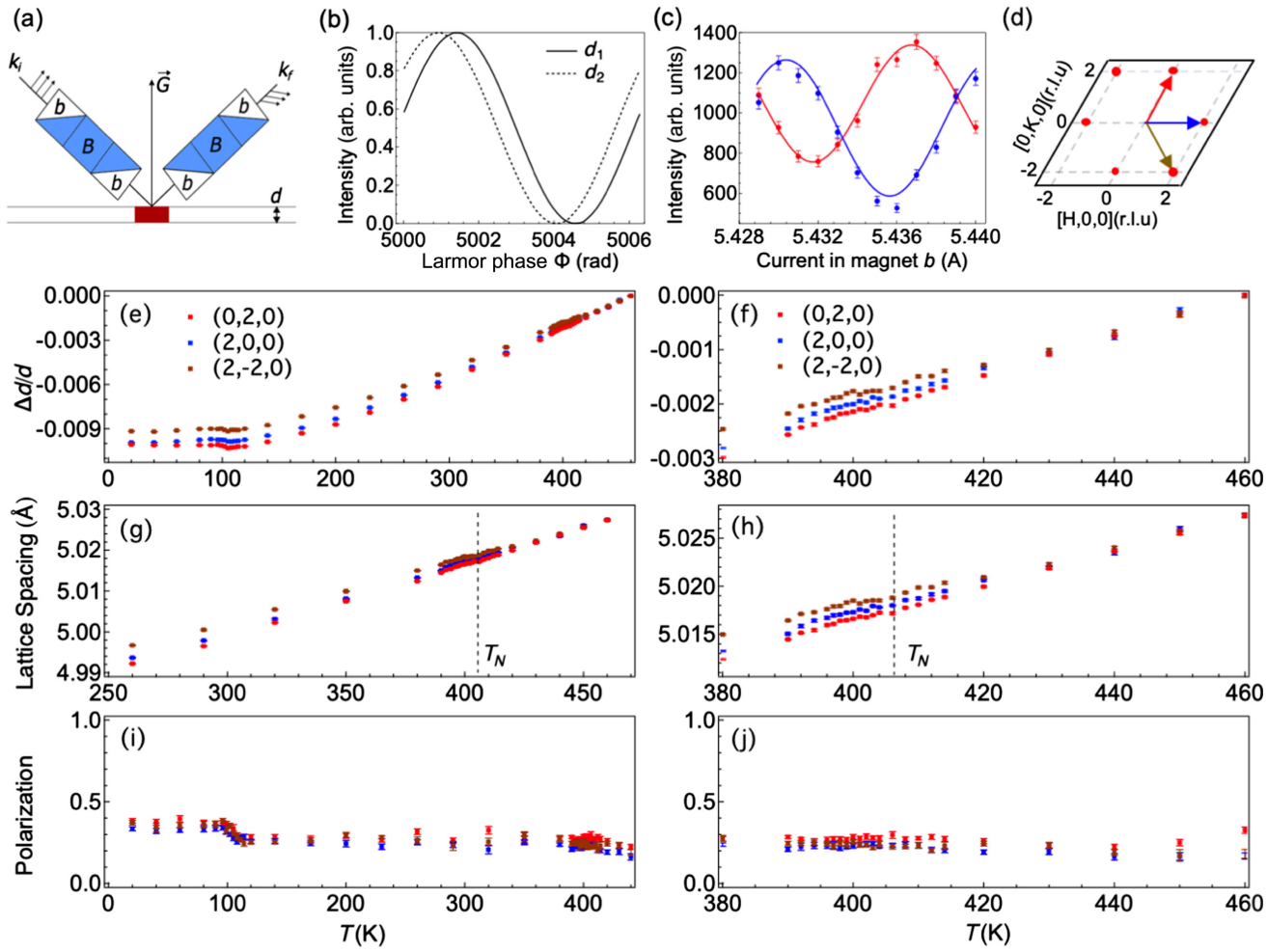

FIG. 2. (a) Schematic of the neutron Larmor diffraction instrument setup with Wollaston prisms. (b) Schematic depicting the Larmor phase difference between two different lattice parameters. (c) Example of raw data taken during neutron Larmor diffraction measurements for the (0, 2, 0) peak, where the red and blue points are 170 K and 20 K, respectively. The solid lines are sinusoidal fits to the data. (d) Schematic of the three lattice Bragg peaks (2, 0, 0), (0, 2, 0), and $(2, -2, 0)$ of the hexagonal phase. (e) $\Delta d/d$ as a function of temperature measured for (0, 2, 0) (red), (2, 0, 0) (blue), and $(2, -2, 0)$ (brown) nuclear Bragg peaks from 20 K to 460 K. (f) Same as panel (a) but for 380 K to 460 K. (g) Temperature dependence of the lattice spacing of three theoretically equivalent Bragg peaks for (0, 2, 0) (red), (2, 0, 0) (blue), and $(2, -2, 0)$ (brown) nuclear Bragg peaks in the $[H, K, 0]$ plane. (h) Expanded view of panel (g) near T_N. The dashed lines in panels (g) and (h) mark the T_N. Since the error bars are smaller than the symbol, they are not visible in panels (e)–(h). (i) Neutron polarization as a function of temperature measured for these three nuclear Bragg peaks from 20 K to 460 K. (j) Same as panel (c) but for 380 K to 460 K.

and we can precisely measure the lattice parameter change above and below twinning. In fact, twinning of the crystal means that multiple Bragg peaks with different lattice parameters occur at approximately the same position in reciprocal space but become broader below the formation of twin domains. Since the lattice parameter correlates linearly with the neutron spin's Larmor phase, an expansion or broadening of the nuclear Bragg peak corresponds to a similar change or dispersion in the neutron spin's Larmor phase. Consequently, any distortion or broadening in the lattice structure and formation of twin domains would manifest as variations in the neutron beam's polarization. This is clearly seen below the Néel temperature of $YBa_2Cu_3O_6$, the AFM-ordered parent compound of cuprate superconductors, in the neutron Larmor diffraction experiment [53]. For FeGe, the observed flatness of neutron polarization across T_N shown in Figs. 2(i) and 2(j) signifies the absence of twinning or broadening during this transition. Surprisingly, the deviation of the three lattice spacing appears slightly above T_N, which extends about 20 K above T_N, as shown in Fig. 2(h). The deviation might be due to the fluctuations of the order parameter above T_N, suggesting a coupling between the magnetism and lattice. The lattice-spacing difference between (2, 0, 0) and $(2, -2, 0)$ at room temperature is about $(d_{2\bar{2}0} - d_{200})/(d_{2\bar{2}0} + d_{200}) \approx 3 \times 10^{-4}$. For comparison, the orthorhombic lattice distortion in NaFeAs pnictide is $(a_o - b_o)/(a_o + b_o) \approx 1.7 \times 10^{-3}$ (where a_o and b_o are

orthorhombic lattice parameters below the structure phase-transition temperature of 58 K), about 5 times larger [52]. Therefore, the AFM phase of FeGe is not an ideal kagome lattice but exhibits a weak lattice distortion around T_N.

Furthermore, nuclear structure factor analysis indicates that the structure factor contribution from the Ge sublattice cancels out in the undistorted hexagonal phase for (2, 0, 0) and its equivalent Bragg peaks. For the distorted lattice, the Ge and Fe atoms' structure factor contributions to the now inequivalent (2, 0, 0), (0, 2, 0), and $(2, -2, 0)$ Bragg peaks are approximately destructive and constructive, respectively (Appendix D). Thus, the distinct three lattice spacing at (2, 0, 0), (0, 2, 0), and (2, −2 0) Bragg peaks suggests the presence of the symmetry-breaking in-plane Fe-sublattice distortions in the kagome plane below T_N.

The threefold symmetry breaking is also revealed in Raman spectroscopy. Above T_N, FeGe has the space group P6/mmm (#191) with three formula units in the unit cell. Fe ions occupy the Wyckoff site $3f$, whereas Ge ions occupy $1a$ (in-plane) and $2d$ (apical) sites. The Γ-point phonon modes transform as $\Gamma_{\text{total}} = 3A_{2u} \oplus B_{2g} \oplus B_{1u} \oplus B_{2u} \oplus E_{2u} \oplus E_{2g} \oplus 4E_{1u}$, where there is only one twofold degenerate Raman-active mode $\Gamma_{\text{Raman}} = E_{2g}(\text{Ge}^2)$ [Ge^2 are the apical Ge ions, which form the honeycomb layer shown in Fig. 1(a)] (Appendix E). In Fig. 3(a), we show the Raman spectra of FeGe at room temperature in the AFM phase. One main phonon at around 160–162 cm^{-1} is detected in all four (XX, XY, RR, and RL) scattering geometries (Appendix A). However, the peak positions in the RR spectrum are at a slightly lower frequency than in the RL spectrum. One mode at 160 cm^{-1} is observed in the RR scattering geometry while a mode at 162 cm^{-1} is observed in the RL scattering geometry. The proximity in energy between these two modes is attributed to their common origin from the splitting of the degenerate Raman-active $E_{2g}(\text{Ge}^2)$ mode of the honeycomb layer in the nonmagnetic phase. The detection of these two split modes indicates threefold rotational symmetry breaking in the AFM phase. The splitting of the $E_{2g}(\text{Ge}^2)$ mode is only 2 cm^{-1} at room temperature, consistent with the rather small lattice distortion observed in the neutron Larmor diffraction measurements shown in Fig. 2(g).

In order to explore the origin of the threefold symmetry breaking in FeGe, we performed first-principles (density functional theory) lattice response calculations to search for the lattice instabilities. The phonon dispersion displays no instabilities when the (collinear) AFM order is imposed in the calculation, which is consistent with Refs. [42,45,48,49]. This finding may be because DFT, being a static mean field theory, typically overestimates the ordered magnetic moments and hence does not correctly capture certain electronic features such as the orbital occupations. When we repeat the DFT calculations without a magnetic order, we find strong instabilities at the Γ and $A(0, 0, 0.5)$ points of the Brillouin zone. In Fig. 3(b), we show these DFT phonon dispersions obtained for the nonmagnetic FeGe with an added on-site Coulomb interaction $U = 2$ eV. A complete branch of the twofold degenerate phonon dispersion that includes Γ_6^- and A_6^- modes has imaginary frequencies, indicating lattice instabilities. The largest imaginary frequency is from the A_6^- mode, and this mode remains unstable in many different configurations (Appendix F). Both of the unstable modes A_6^- and Γ_6^- can lead to either orthorhombic or monoclinic structures: A_6^- can drive a transition to space groups Cmcm (#63, point group D_{2h}) or $\text{P2}_1/\text{m}$ (#11, point group C_{2h}), and Γ_6^- can lead to space groups Amm2 (#38) or Pm (#6). Details of the group-subgroup analysis are presented in

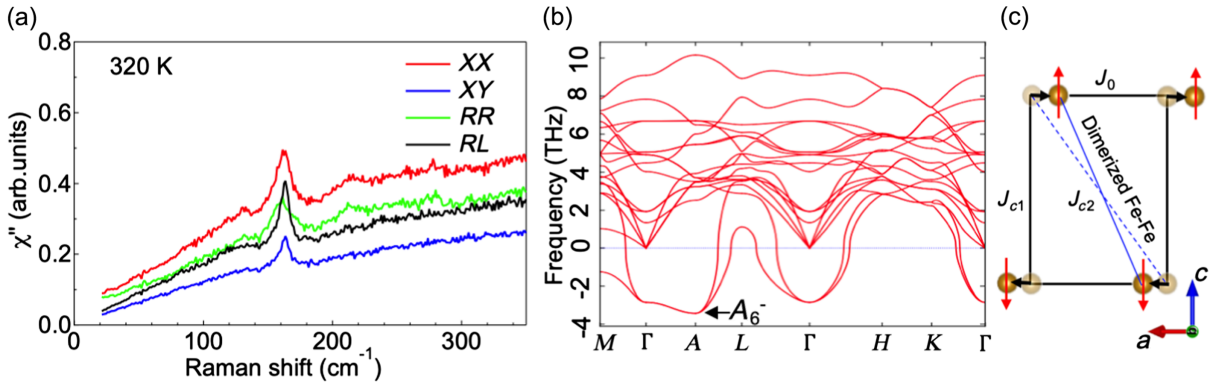

FIG. 3. (a) Raman spectra in the XX, XY, RR, and RL scattering geometries at 320 K. (b) DFT phonon dispersion calculation for FeGe in the nonmagnetic phase with $U = 2$ eV and spin not included. The black arrow indicates the A_6^- lattice instability. The high-symmetry k points follow the conventional notation of the hexagonal Brillouin zone. (c) Illustration of Fe displacements following the A_6^- lattice instability in a Fe-Fe lattice from the ac plane. Ge atoms are omitted for simplification. The black arrows represent the Fe displacement directions while the red arrows represent the spin ordering. In-plane exchange energy is labeled as J_0, and the nearest and next-nearest exchange energy along the c axis are labeled as J_{c1} and J_{c2}, respectively. The two Fe-Fe connected by J_{c2} with opposite spin orientations may form a dimerlike singlet due to the A_6^- displacements.

Appendix G. The main difference between A_6^- and Γ_6^- is that A_6^- leads to a doubling of the unit cell along the c-axis direction while Γ_6^- does not because A_6^- has the same wave vector as the collinear A-type AFM order. While we explicitly focus on the A_6^- mode in the rest of this paper, a similar argument also applies to the Γ_6^- mode, and we cannot distinguish these different structures driven by A_6^- or Γ_6^- instabilities within the resolution of the present Raman data (Appendix G). The monoclinic and orthorhombic structures below T_N that the A_6^- mode leads to are illustrated in Figs. 1(b) and 1(c), respectively.

The symmetry breaking at T_N driven by the A_6^- lattice instability mainly involves displacements of Fe or Ge[1] in the kagome layer. The resulting displacements have opposite directions for the top and bottom kagome layers (Appendix H). Thus, the Ge[2] atoms in the honeycomb layer experience an anisotropy of the local crystal electrical field [Fig. 1(b)]. As a consequence, the fundamental $E_{2g}(\mathrm{Ge}^2)$ mode from the honeycomb layers splits into $A_g \oplus B_g$ (C_{2h} point group) for the monoclinic AFM phase. This explains the two modes we observed at room temperature shown in Fig. 3(a). The mode observed in the *RR* scattering geometry is attributed to the A_g mode while the one observed in the *RL* scattering geometry is attributed to the B_g mode (Appendix I). Illustrations of the A_g and B_g lattice vibration patterns for the Ge[2] atoms are shown in Figs. 1(e) and 1(f), respectively.

B. CDW phase

Below 110 K, FeGe undergoes a CDW transition [39]. Recent x-ray studies show that the crystal structure of the $2 \times 2 \times 2$ CDW phase is associated with the c-axis dimerization of Ge[1] atoms in the kagome layer of FeGe [Fig. 1(g)] based on Refs. [42,43]. New phonon modes are expected to appear in the CDW state due to Brillouin zone folding [54]. Only those modes modulating the ionic deviation above T_{CDW} with a large amplitude can obtain noticeable Raman intensity below T_{CDW} and thus can be detected in the Raman spectra [55–57]. In Fig. 4(a), we show several new phonon modes appearing in all four scattering geometries at 90 K in the CDW state. Specifically, four additional modes are detected in the *RR* scattering geometry, and eight additional modes are observed in the *RL* scattering geometry below T_{CDW}. These modes are the amplitude modes of the CDW order parameter. These new phonon peak positions are summarized in Appendix J.

In the inset of Fig. 4(a), we show the Raman response in both *RR* and *RL* scattering geometries up to 900 cm^{-1} for above and below T_{CDW}. The CDW gap-opening signatures, namely, the suppression of the low-energy spectra weight and the enhancement of the spectra weight close to $2\Delta \approx 50$ meV determined by STM [40,43] and ARPES [41], are not observed in the Raman response. The absence

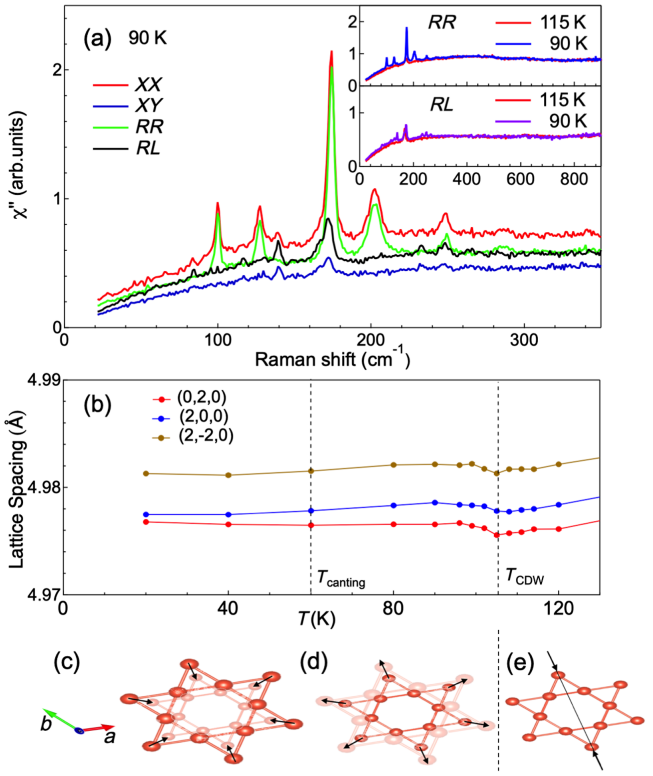

FIG. 4. (a) Raman spectra in the *XX*, *XY*, *RR*, and *RL* scattering geometries at 90 K. The inset of panel (a) shows the Raman response in the *RR* (top panel) and *RL* (bottom panel) scattering geometries in an extended energy range up to 900 cm^{-1} at 115 K and 90 K. (b) Temperature dependence of the d-spacing of three Bragg peaks for (0, 2, 0) (red), (2, 0, 0) (blue), and $(2, -2, 0)$ (brown) nuclear Bragg peaks in the $[H, K, 0]$ plane below 130 K. The dashed lines in panel (b) mark T_{CDW} and T_{canting}. (c)–(e) Schematic of lattice distortion observed using neutron Larmor diffraction for temperatures above T_{CDW} and below T_{CDW}. Above T_{CDW}, panel (e) illustrates the monoclinic lattice distortion. Below T_{CDW}, the lattice first displays a negative thermal expansion, and the unit-cell volume becomes larger, as shown in panel (d). Upon further cooling below T_{CDW}, the unit-cell volume then becomes smaller again, as shown in panel (c). The kagome lattices shown in panels (c)–(e) are depicted in real space with exaggerated distortions for visual clarity.

of CDW gap-opening signatures may be due to the multiband effects in FeGe, similar to the AV_3Sb_5 system [58].

After establishing the Raman spectroscopic signature of the CDW state, we present the lattice response data below T_{CDW}. In Fig. 4(b), we show the temperature dependence of the three lattice spacings upon cooling across T_{CDW}. In the AFM phase above T_{CDW}, the unit cell is monoclinic, as illustrated in Fig. 4(e). The three lattice spacings decrease upon cooling, following the normal thermal expansion rule. Below T_{CDW}, the three lattice spacings display anomalies and increase upon cooling, indicating a small negative thermal expansion, as illustrated in Fig. 4(d). Upon further cooling, the three

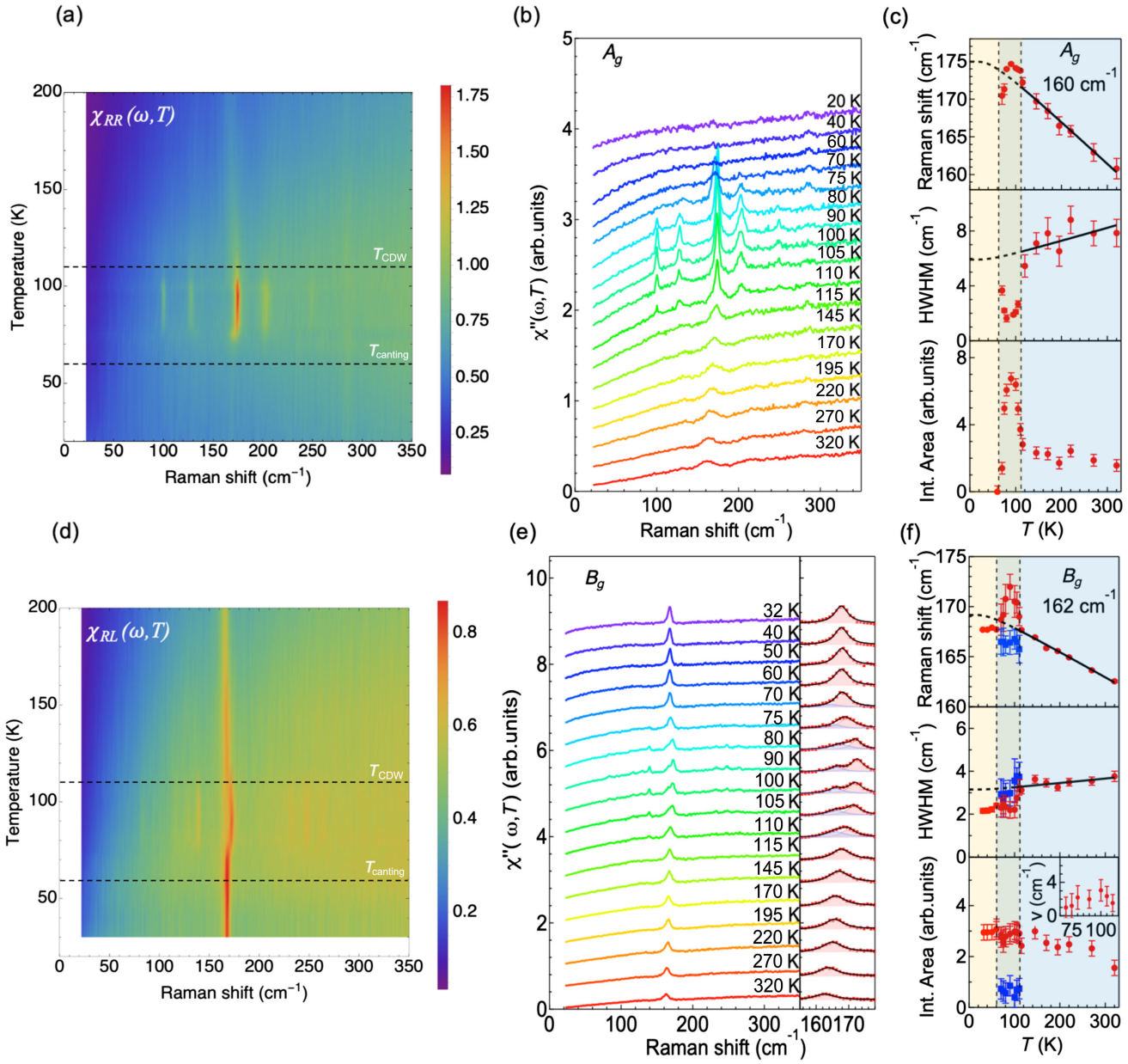

FIG. 5. (a) Color plot of the T dependence of Raman response in the RR scattering geometry for FeGe. (b) Corresponding Raman spectra of panel (a). (c) T dependence of the peak position, half width at half maximum (HWHM), and integrated intensity for the A_g phonon mode at 160 cm^{-1}. The error bars represent 1 standard deviation. The T dependence of phononic frequency and HWHM are fitted by an anharmonic phonon decay model (Appendix M). The dashed lines in panels (a) and (c) represent T_{CDW} and T_{canting}. (d) Color plot of the T dependence of Raman response in the RL scattering geometry for FeGe. (e) Corresponding Raman spectra of panel (d). The right part of panel (e) shows a zoom-in of the T dependence of the B_g phonon mode at around 162 cm^{-1} and its low-energy shoulder peak. The black solid lines are the fitting curve for the total coupled response. The red and blue shaded areas represent the two bare modes. (f) T dependence of the peak position, HWHM, and integrated intensity for the bare B_g phonon mode at around 162 cm^{-1} (red) and the bare shoulder peak (blue). The inset in the bottom panel of (f) is the fitted interaction strength between the bare B_g phonon mode at 162 cm^{-1} and the bare shoulder peak. The error bars represent 1 standard deviation. The T dependence of phononic frequency and HWHM are fitted by an anharmonic phonon decay model (Appendix M).

lattice spacings decrease again, and the unit-cell volume become smaller, as we illustrate in Fig. 4(c). To our surprise, the difference between the lattice spacing for the lattice Bragg peaks (0, 2, 0) and (2, 0, 0) become smaller and smaller and tend to be almost the same size at the lowest temperature 20 K. This finding indicates that the monoclinic lattice distortion is weakened and that the lattice tends to be orthorhombic at low temperatures

(Appendix C), signifying that the lattice symmetry tends to ascend at low temperatures.

The weakening of the monoclinic lattice distortion below T_{CDW} is also seen from the temperature dependence of the Raman modes. In Figs. 5(a) and 5(b), we present the T dependence of the phonon modes in the RR scattering geometries. The phonon modes at 100 cm^{-1}, 127 cm^{-1}, 203 cm^{-1}, and 249 cm^{-1} appear abruptly below T_{CDW}. In contrast, the A_g phonon at 160 cm^{-1} continuously evolves into the CDW phase. As shown in Fig. 5(c), the mode hardens and sharpens upon cooling and experiences additional hardening and sharpening below T_{CDW}. However, it softens and broadens when approaching $T_{canting}$ and finally disappears below $T_{canting}$. The broadening of the Raman modes when approaching $T_{canting}$ is also found for the other three modes at 100 cm^{-1}, 127 cm^{-1}, and 203 cm^{-1} in the RR scattering geometry of the CDW phase (Appendix K). Remarkably, the integrated intensity for the A_g phonon at the 160 cm^{-1} mode is enhanced 3.5 times below T_{CDW} but decreases to zero close to $T_{canting}$. In Figs. 5(d) and 5(e), we present the T dependence of the phonon modes in the RL scattering geometries. The B_g phonon at 162 cm^{-1} persists from room temperature down to 32 K. In contrast, several new modes appear in the CDW phase and disappear below $T_{canting}$. In particular, a shoulder peak develops on the lower-energy side of this phonon below T_{CDW}, as is shown in a zoom-in plot on the right part of Fig. 5(e). The mode at 162 cm^{-1} and the shoulder mode can be described by a coupled two-Lorentzian-phonon model on a linear background (Appendix L), as shown in Fig. 5(e). In Fig. 5(f), the B_g mode at 162 cm^{-1} hardens and sharpens upon cooling and experiences additional hardening and sharpening below T_{CDW}. It softens sharply when approaching $T_{canting}$ and barely changes below $T_{canting}$. The weakening and disappearance of the A_g mode at 160 cm^{-1} in the RR scattering geometry and a single peak at 162 cm^{-1} recovering in the RL scattering geometry below $T_{canting}$ indicate that the monoclinic lattice distortion is weakened at lower temperatures. It might be too weak to give rise to any noticeable Raman intensity in the RR scattering geometry.

III. DISCUSSION AND CONCLUSION

The A_6^- lattice instability mainly involves in-plane Fe or Ge^1 displacements in the kagome layer, leading to the threefold symmetry breaking. The in-plane Fe displacement was revealed in a recent x-ray refinement study, though it is not an A_6^- type yet [44]. The degenerate fundamental $E_{2g}(Ge^2)$ mode in the nonmagnetic phase splits into two modes below T_N due to the symmetry breaking. However, we do not detect any additional noticeable phonon intensity related to the Fe or Ge^1 vibration modes in the Raman spectra at room temperature, as shown in Fig. 3(a). We note that the x-ray scattering measurement did not detect the dimerization lattice Bragg peak at $(H, K, L + 0.5)$ (H, K, L are integers) between T_N and T_{CDW} [42,44]. This finding might be due to the small amplitude of the in-plane Fe and Ge^1 displacements, as the monoclinic lattice distortion is close to 0.03% at room temperature [Fig. 2(g)], or the fact that the in-plane A_6^- displacements do not modulate the distance between the layers.

The neutron Larmor diffraction results [Fig. 2(g)] indicate in-plane lattice distortion in the kagome plane in the AFM ordered phase. Furthermore, recent inelastic neutron scattering results show that the spin-wave dispersion along the c-axis direction displays a spin gap of about 1 meV at room temperature at (0, 0, 0.5) [59]. The AFM order below T_N, accompanied by in-plane lattice distortion and a spin-gap opening in the magnetic excitation spectrum, suggests that the AFM transition at T_N is a likely spin-Peierls-like transition driven by spin-lattice coupling [60]. Indeed, as we show in Fig. 3(c), the A_6^- lattice instability displaces the Fe atoms in opposite directions for two adjacent kagome planes, thus modulating the interlayer Fe-Fe distance. In particular, the two Fe-Fe distance connected by next-nearest exchange energy J_{c2} becomes shorter and may possibly form a dimerlike singlet, creating the spin gap and spontaneously aligning the moment along the c-axis direction. The existence of such a spin gap could lead to a decrease in magnetic free energy that outweighs the increase in lattice free energy due to the distortion [61,62]. Thus, a compete understanding of the AFM transition at T_N needs to treat the A_6^- lattice displacements, magnetic interactions, and spin-lattice coupling on equal footing.

The neutron Larmor diffraction results [Fig. 2(g)] reveal in-plane lattice distortions $(d_{200} - d_{020})/(d_{200} + d_{020}) \sim 0.02\%$ and $(d_{2\bar{2}0} - d_{200})/(d_{2\bar{2}0} + d_{200}) \sim 0.04\%$ in the kagome plane of the AFM ordered phase at around 110–115 K, with an average lattice distortion of about 0.03%. The corresponding split-phonon anisotropy for the A_g and B_g modes is $(\omega_{A_g} - \omega_{B_g})/(\omega_{A_g} + \omega_{B_g}) = (172 - 168)/(172 + 168) = 1.2\%$, which is about 40 times that of the lattice anisotropy. In comparison, the AFM phase of $EuFe_2As_2$ has a split-phonon anisotropy of about 4% and a lattice distortion of about 0.55% at 30 K [63]. The ratio between split-phonon anisotropy and the lattice distortion is about 7 for $EuFe_2As_2$. The larger ratio between split-phonon anisotropy and the lattice distortion in FeGe suggests additional interactions such as spin-lattice (spin-phonon) coupling play an important role in creating a large split-phonon anisotropy with a tiny lattice distortion [64].

The CDW phase evolves from the monoclinic AFM phase. Since the monoclinic lattice distortion is about 0.03% at room temperature, we can thus approximately regard the monoclinic AFM phase as a hexagonal lattice

with a weak monoclinic lattice distortion as a perturbation. In this case, the CDW phase could be approximately driven by three L-point lattice instabilities of the hexagonal lattice, leading to a $2 \times 2 \times 2$ reconstruction of the AFM phase. Below T_{CDW}, the CDW order parameter coexists with the monoclinic lattice distortion, persisting to the lowest temperature, and it does not show any noticeable changes upon cooling across T_{canting} [39]. From Fig. 4(b), the monoclinic lattice distortion is already weakened well above T_{canting} in the CDW phase. Similarly, from Fig. 5(c), the A_g mode at 160 cm^{-1} starts to weaken and broaden below 90 K, which is also above T_{canting} in the CDW phase. The temperature dependence of the CDW order parameter and the monoclinic lattice distortion suggests that the A_6^- monoclinic lattice distortion is weakened by coupling to the CDW order parameter. We note that the spin-canting order parameter could also be coupled to the A_6^- order parameter and help weaken the monoclinic lattice distortion. Thus, both coupling mechanisms could contribute to weakening the monoclinic lattice distortion, leading to the lattice symmetry ascending at lower temperatures. One possible scenario to explain the Raman data below T_{canting} is that the lattice symmetry recovers to the hexagonal symmetry, which prohibits the splitting between the A_g mode at 160 cm^{-1} and the B_g mode at 162 cm^{-1}. This scenario differs from the lattice constant data from Larmor diffraction, where FeGe tends to become orthorhombic when approaching 10 K. We note that the Raman phonon intensity in FeGe is generally 2 orders of magnitude weaker than that in the AV_3Sb_5 compound [58]. The weak Raman signal makes the study of Raman phonons rather challenging in FeGe. The origin of these sharp changes in the Raman data close to T_{canting} is an open question and calls for future investigation.

The interplay between the A_6^- monoclinic lattice distortion, CDW, and spin-canting order parameters can be captured by a phenomenological free energy model constructed in the nonmagnetic hexagonal P6/mmm phase with the highest symmetry. The free energy of FeGe in terms of the unstable A_6^- mode (two dimensional, with components A_i, $i = 1, 2$), the L-point bond-order CDW modes (either L_2^- or L_1^+ depending on the origin choice, with components L_i, $i = 1, 2, 3$), and the spin-canting order parameter S is the collection of all polynomials that are invariant under all symmetry operations of the parent space group. It can be written up to fourth order as

$$\mathcal{F} = \mathcal{F}_A + \mathcal{F}_L + \mathcal{F}_{AL} + \mathcal{F}_S + \mathcal{F}_{AS}, \tag{1}$$

$$\mathcal{F}_A = \alpha_A A^2 + \beta_A A^4, \tag{2}$$

$$\mathcal{F}_L = \alpha_L L^2 + \beta_L L^4 + \lambda_L (L_1^2 L_2^2 + L_2^2 L_3^2 + L_3^2 L_1^2), \tag{3}$$

$$\mathcal{F}_{AL} = \lambda_{AL} A^2 L^2 + \gamma_{AL} \left[A_1^2 \left(\frac{5}{6} L_1^2 + \frac{2}{6} L_2^2 + \frac{5}{6} L_3^2 \right) + A_2^2 \left(\frac{1}{2} L_1^2 + L_2^2 + \frac{1}{2} L_3^2 \right) + \frac{1}{\sqrt{3}} A_1 A_2 (-L_1^2 + L_3^2) \right], \tag{4}$$

$$\mathcal{F}_S = \alpha_S S^2 + \beta_S S^4, \tag{5}$$

$$\mathcal{F}_{AS} = \lambda_{AS} A^2 S^2. \tag{6}$$

There is no third-order coupling between A_i and L_i. Even though the fourth-order couplings between the two order parameters A and L are not isotropic, the generic biquadratic coupling term λ_{AL} is sufficient to explain the competition between A and L order parameters. The second-order coefficient of A is renormalized when L is nonzero according to $F_A = (\alpha_A + \lambda_{AL} L^2) A^2 + \beta_A A^4$. If $\lambda_{AL} > 0$, the CDW order parameter L_2^- (or L_1^+) would suppress A_6^- and make the monoclinicity disappear eventually.

Since the spin-canting order parameter S transforms as a time-reversal odd irreducible representation at the incommensurate wave vector, it can couple with the A order parameter only at the biquadratic level or higher. Since the monoclinic distortion is small, its energy scale can be comparable to that of the spin-canting order in FeGe; in other words, $|\alpha_A| \sim |\lambda_{AS} S^2|$. This finding would explain that, as the spins are canted at low temperature, its monoclinicity is weakened because the additional competition between S and A would help suppress the A order parameter.

Setting $\alpha_A(T) = \alpha_{A_0}(T - T'_{\mathrm{N}})$, $\alpha_L(T) = \alpha_{L_0}(T - T'_{\mathrm{CDW}})$, and $\alpha_S(T) = \alpha_{S_0}(T - T'_{\mathrm{canting}})$, where T'_{N}, T'_{CDW}, and T'_{canting} are the phase-transition temperatures without the coupling terms, and minimizing the free energy in Eq. (1) with respect to A, L, and S, we obtain the solution of the T dependence of $A(T)$, $L(T)$, and $S(T)$. While it is not possible to determine the parameters of the free energy precisely, we could choose a combination that reproduces the experimental observations. There are other possibilities with different contributions from the CDW or incommensurate magnetic order parameter that suppress the monoclinic lattice distortions at low temperatures. For illustration purposes, we choose the parameters to reproduce the transition temperatures, and the fact that the lattice anisotropy (here represented by the A order parameter) is suppressed by both the CDW and the incommensurate magnetic order parameters. As we show in Fig. 6, positive coupling constants λ_{AL} and λ_{AS} weaken the monoclinic distortion and make it disappear below T_{canting}. Other possibilities describing the interplay between A and L order parameters may involve the γ_{AL} term, which prefers a certain direction of A order parameters depending on the direction of L order parameters.

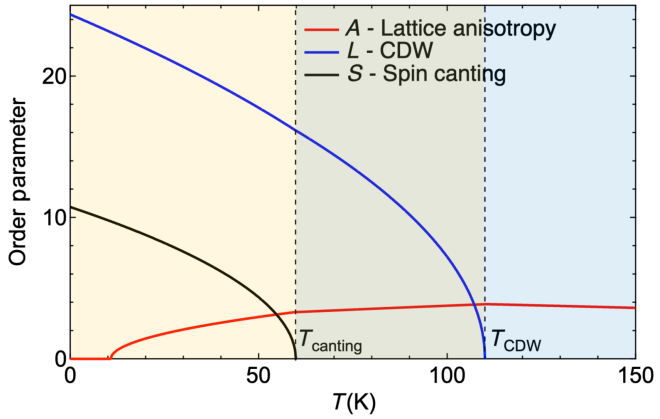

FIG. 6. Illustration of the Landau free energy model in Eq. (1). The parameters used in the model are $\alpha_{A_0} = 0.1$, $\beta_A = 1$, $\alpha_{L_0} = 0.1$, $\beta_L = 0.01$, $\lambda_{AL} = 0.05$, $\lambda_L = 0$, $\gamma_{AL} = 0$, $\alpha_{S_0} = 0.2$, $\beta_S = 0.06$, $\lambda_{AS} = 0.14$, $T'_{\mathrm{N}} = 410$, $T'_{\mathrm{CDW}} = 117.5$, and $T'_{\mathrm{canting}} = 67.5$. The red, blue, and black solid lines represent the T dependence of the order parameters A, L, and S, respectively. The two dashed lines represent T_{CDW} and T_{canting}. The blue and yellow shaded areas represent the AFM phase ($T_{\mathrm{canting}} < T < T_{\mathrm{N}}$) and the CDW phase ($T < T_{\mathrm{CDW}}$), respectively.

The interplay between the A_6^- monoclinic lattice distortion, CDW, and magnetic order originates from the fact that they are competing orders with similar energy scales. This case is similar to the C_4 reentrance phase observed in the hole-doped iron pnictides, where the formation of an out-of-plane collinear double-**Q** magnetic ordering [7,8,11,12,65] leads to the restoration of lattice symmetry from orthorhombic to tetragonal upon cooling due to competing orders [13,14]. The difference is that the weakening of the A_6^- monoclinic lattice distortion is a gradual process in FeGe while it is more drastic in iron-based superconductors. It originates from the different nature of the phase transition involved in the symmetry ascending, namely, the second-order-like phase transition in FeGe while it is first-order-like in iron-based superconductors.

We note that the CDW-related phonon modes disappear in the CDW phase, and they cannot be explained by the phenomenological model of the A_6^- mode and spin-canting interplay. One possible interpretation of the disappearing CDW-related phonon modes is their coupling to incommensurate spin fluctuations. From our inelastic neutron scattering experiments on FeGe, we find that the intensities of the low-energy incommensurate spin fluctuations do not follow the Bose population factor below T_{CDW}. Instead, they are enhanced dramatically below T_{CDW} [59]. Although it is unclear why the CDW-induced phonons would disappear in the incommensurate magnetic ordered phase, it is possible that a coupling between the incommensurate static order and lattice can induce a secondary lattice instability below T_{canting}. As Raman scattering is a $Q = 0$ probe, any small deviation from commensurate positions would have a large impact on Raman scattering results, but it would not dramatically influence the neutron and x-ray scattering results.

Compared with all the other kagome magnets, FeGe possesses magnetic order, CDW order, and strong interactions between magnetic and CDW order [39]. The CDW can also be tuned by a simple annealing process where the correlation length of CDW can change from 0 to 100% [43,44,66]. Beyond kagome systems, to the best of our knowledge, we are not aware of other CDW materials where the CDW can have such a strong coupling with magnetism and the CDW can also be tuned. Thus, determining the symmetry of the crystal structure of FeGe is the very first step in sorting out the rich electronic and magnetic properties of this system.

The experimental observations in FeGe provide a rather rare type of spin-lattice coupling because the collinear A-type AFM structure is not expected to have an impact on the kagome lattice structure, particularly the in-plane crystal structure. We have shown that FeGe displays a series of structural phase transitions in the magnetic ordered phase, including threefold rotational symmetry breaking at T_{N}, a CDW transition, negative thermal expansion, and a tendency of symmetry ascending at lower temperatures in the spin-canting phase, which are all directly related to the in-plane lattice distortion in the kagome structure. In particular, the lattice distortion is on the order of 10^{-4}; such a small lattice distortion is observed both by Raman and phase-sensitive Larmor neutron techniques. In general, the energy scale of the crystal structural distortions is much larger than the magnetic exchange energy and spin-orbit coupling strength, as seen in cuprates, nickel oxides, and iron pnictides. FeGe seems to be a rare case where magnetic, lattice, and spin-orbit coupling energy scales are similar, resulting in their interaction and interplay. This finding renders FeGe an interesting system where an extremely weak structural instability breaks the threefold symmetry, coexists, and competes with the CDW and magnetic orders. The unusual intertwined orders between spin, charge, and lattice degrees of freedom unveiled here may arise from the correlated electron effect of flattish electronic bands [41].

ACKNOWLEDGMENTS

We acknowledge useful discussions with Hengxin Tan and Binghai Yan. The spectroscopic work conducted at Rutgers (S.-F. W. and G. B.) was supported by the National Science Foundation (NSF) Grant No. DMR-2105001. The neutron scattering and single crystal synthesis work at Rice was supported by Grant No. NSF-DMR-2100741 and by the Robert A. Welch Foundation under Grant No. C-1839, respectively (P. D.). The theoretical work conducted at the University of Minnesota (J. S., E. R., and T. B.) was supported by the NSF CAREER Grant No. DMR-2046020. X. K. T. and M. Y. are partially supported by the Robert A. Welch Foundation Grant No. C-2175, and the Gordon and Betty Moore Foundation's EPiQS Initiative through Grant No. GBMF9470. The work at NICPB was supported by the

European Research Council (ERC) under the European Unions Horizon 2020 research and innovation program Grant Agreement No. 885413. A portion of this research used resources at the Spallation Neutron Source and High Flux Isotope Reactor, DOE Office of Science User Facilities operated by ORNL. The development of the Larmor diffraction technique was supported by the U.S. Department of Energy, Office of Science, Office of Basic Energy Sciences, Early Career Research Program Award (KC0402010), under Contract No. DE-AC05-00OR22725.

APPENDIX A: METHODS

1. Single crystal preparation and characterization

Single crystals of FeGe were synthesized via the chemical vapor transport method described in Ref. [39], and the chemical compositions were determined by x-ray refinement [39]. These samples were characterized by electric transport and magnetic susceptibility measurements. The extracted collinear A-type antiferromagnetic phase-transition temperature T_N, CDW transition temperature (T_{CDW}), and spin-canting transition temperature (T_{canting}) for FeGe were about 400, 110, and 60 K, respectively [39]. The sharpness of the Raman modes and the low residual spectra background (Fig. 5) indicate the high quality of the single crystals.

2. Raman scattering measurements

The as-grown FeGe sample with the (0 0 1) surface was positioned in a continuous-helium-flow optical cryostat. The Raman data shown in the main text are obtained from this sample. A polished (0 0 1) surface and an as-grown (1 0 0) surface of the FeGe crystals were also studied, and they showed consistent results. The Raman measurements were mainly performed using the Kr^+ laser line at 647.1 nm (1.92 eV) in a quasibackscattering geometry along the crystallographic c axis. The excitation laser beam was focused into a 50×100 μm^2 spot on the ab surface, with an incident power around 17 mW. The scattered light was collected and analyzed by a triple-stage Raman spectrometer and recorded using a liquid-nitrogen-cooled charge-coupled detector. Linear and circular polarizations were used in this study to decompose the Raman data into different irreducible representations. The instrumental resolution was maintained better than 1.5 cm^{-1}. All linewidth data presented were corrected for the instrumental resolution. The temperatures shown in this paper were corrected for laser heating (Appendix B).

All spectra shown were corrected for the spectral response of the spectrometer and charge-coupled detector to obtain the Raman intensity $I_{\mu\nu}$, which is related to the Raman response $\chi''(\omega, T)$: $I_{\mu\nu}(\omega, T) = [1 + n(\omega, T)]\chi''_{\mu\nu}(\omega, T)$. Here, $\mu(v)$ denotes the polarization of the incident (scattered) photon, ω is the energy, T is the temperature, and $n(\omega, T)$ is the Bose factor.

The Raman spectra were recorded from the ab (0 0 1) surface for scattering geometries denoted as $\mu\nu = XX, XY, RR, RL$, which is short for $Z(\mu\nu)\bar{Z}$ in Portos notation, where X and Y denote linear polarization parallel and perpendicular to the crystallographic a or b axis, respectively, and $R = X + iY$ and $L = X - iY$ denote the right- and left-circular polarizations, respectively. The Z direction corresponds to the c-axis direction perpendicular to the (0 0 1) plane.

3. Neutron Larmor diffraction measurement

Neutron Larmor diffraction measurements were performed on the HB-1 polarized triple axis spectrometer of the High Flux Isotope Reactor (HFIR) at Oak Ridge National Laboratory (ORNL), USA. We used a single crystal (about 100 mg) mounted inside a closed-cycle refrigerator with an operating temperature range between 20 and 460 K. It is a bulk measurement and probes the entire sample. The momentum transfer $\mathbf{Q}$ in 3D reciprocal space in $Å^{-1}$ was defined as $\mathbf{Q} = H\mathbf{a}^* + K\mathbf{b}^* + L\mathbf{c}^*$, where H, K, and L are Miller indices with $\mathbf{a} = a\hat{\mathbf{x}}$, $\mathbf{b} = b(\cos 120\hat{\mathbf{x}} + \sin 120\hat{\mathbf{y}})$, and $\mathbf{c} = c\hat{\mathbf{z}}$ ($a \approx b \approx 4.99$ Å, $c \approx 4.05$ Å at room temperature). Although this definition of an ideal kagome lattice structure, strictly speaking, is only valid above T_{N}, we use this notation throughout the paper as the in-plane lattice distortion is small enough that it does not affect the discussion.

4. Density functional theory calculations

DFT calculations were performed within the Perdew-Burke-Ernzerhof-type generalized gradient approximation [67], which is implemented in the Vienna *Ab initio* Simulation Package (VASP) [68,69] using the experimental crystal structure. The projected augmented wave potentials with nine valence electrons for the Fe atom and five valence electrons for Ge were employed. The cutoff energy for the plane-wave basis set was 300 eV. The zero-damping DFT-D3 van der Waals correction was employed throughout the calculations. The phonon dispersion was calculated by using the finite displacement method as implemented in the phonopy code [70]. The on-site Coulomb interaction U was set to 2 eV for Fig. 3(b). For the phonon calculation in the nonmagnetic phase, we did not introduce a magnetic order.

Group theory predictions were performed using the tool provided in the Isotropy Software Suite and the Bilbao Crystallographic Server [71–73]. The information for the irreducible representations of point groups and space groups follow the notations of Cracknell, Davies, Miller, and Love [74].

APPENDIX B: LASER HEATING DETERMINATION

The laser heating rate, a measure of the temperature increase per unit laser power (K/mW) in the focused laser spot, in the Raman experiments was determined by

TABLE I. Cryostat temperature T_0, laser spot temperature T_{spot}, laser heating ΔT, and heating coefficient k for FeGe at different temperatures with a constant laser power of $P = 17$ mW.

T_0 (K)	T_{spot} (K)	ΔT (K)	k (K/mW)
10	42.5	32.5	1.91
20	46.6	26.6	1.56
40	60.8	20.8	1.22
90	110	20	1.18
150	172	22	1.29
200	223	23	1.35
300	323	23	1.35

monitoring the appearance of new phonon modes induced by the CDW order during the cooling process with a constant laser power of 17 mW.

At the cryostat temperature 95 K, we barely detect any new phonon modes, indicating the laser spot temperature is above $T_{\text{CDW}} = 110$ K. When cooling the sample to 90 K, we start to detect several weak new-phonon signals both in the *RR* and *RL* scattering geometries, indicating the laser spot temperature is slightly below 110 K. When cooling the sample to 85 K, the intensity of these new modes develops significantly, indicating the laser spot temperature is well below 110 K. Thus, the heating coefficient can be determined via $90\ \text{K} + 17\ \text{mW} * \text{k} \approx 110\ \text{K}$. In this way, we have deduced the heating coefficient $k \approx 1.2 \pm 0.1$ K/mW.

We note that the heating coefficient k is not a constant with cooling. The T dependence of the heating coefficient k can be estimated by solving the heat transfer equation. The thermal conductivity, incident laser power P, and temperature of interest inside the laser spot T_{spot} are connected by the integral equation [75,76]

$$\int_{T_0}^{T_{\text{spot}}} \kappa(T)dT = \frac{P \cdot d^*}{S} = \text{constant}, \tag{B1}$$

where T_0 is the cold helium-gas temperature where the sample is located in the cryostat, S is the area of the laser spot, and d^* is an effective thickness. The constant $P \cdot d^*/S$ can be determined by a single measurement of a distinctive temperature in the laser spot, as we did at $T_0 = 90$ K, where $T_{\text{spot}} = 110$ K.

Since the thermal conductivity data of FeGe are not available in the literature, we estimated it from the measured in-plane electric conductivity data $\sigma(T)$, which is connected by the in-plane resistivity as $1/\rho(T)$ [39]. Based on the Wiedemann-Franz law for a simple metal, the thermal conductivity $\kappa(T)$ can by approximated by $\sigma(T) * T * L_0$, where L_0 is the Lorenz number 2.44×10^{-5} mWK^{-2}. We note that the Wiedemann-Franz law is generally valid for high temperatures and for low (i.e., a few Kelvins) temperatures but may not hold at intermediate temperatures [77]. Nevertheless, we roughly estimate the T-dependent heating coefficient assuming that $L_0 = \kappa(T)/(\sigma(T) * T)$ is a constant for FeGe. The estimated T-dependent heating coefficients are shown in Table I.

For $T_0 = 10$ K and 20 K, the heating coefficient changes substantially (less than 1.6 times) compared with $T_0 = 90$ K. For a wide temperature range from $T_0 = 20$ K to 300 K, the heating coefficient does not vary much compared with $T_0 = 90$ K.

APPENDIX C: SIMULATION OF THE LATTICE BRAGG PEAKS IN MOMENTUM SPACE

In this appendix, we present the simulation of the three lattice Bragg peaks (2, 0, 0), (0, 2, 0), and $(2, -2, 0)$ in the $k_z = 0$ momentum space for FeGe. These three lattice Bragg peaks correspond to three lattice spacings in real space as shown in Fig. 2(g). The simulation is performed using the ISODISTORT program from the ISOTROPY Software Suite [78,79].

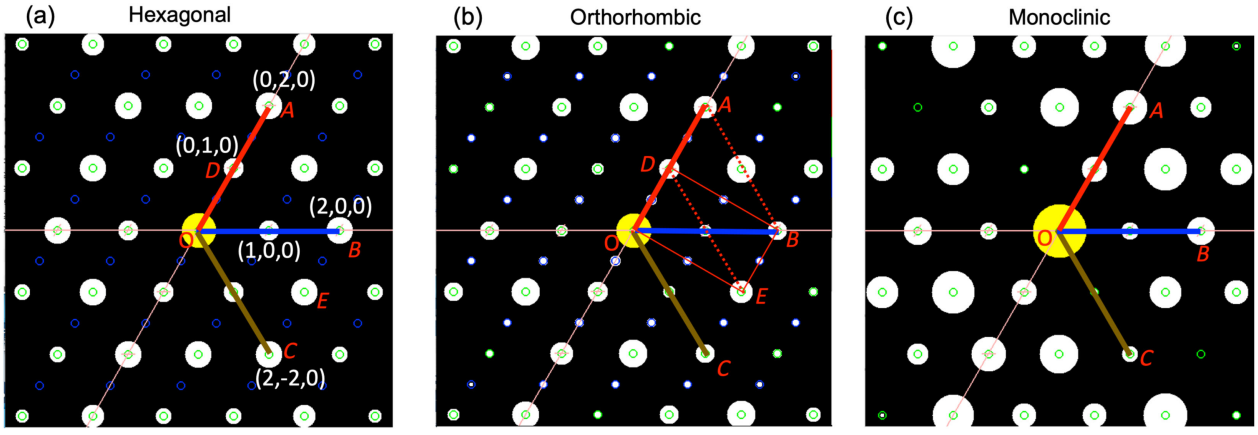

FIG. 7. Lattice Bragg peaks simulation in momentum space for the hexagonal phase (a), orthorhombic phase (b), and monoclinic phase (c) in the $k_z = 0$ plane using the ISODISTORT program from ISOTROPY Software Suite [78,79]. The Lattice Bragg peaks (0, 2, 0), (2, 0, 0), $(2, -2, 0)$, (0, 1, 0), $(2, -1, 0)$, and (0, 0, 0) are represented by *A*, *B*, *C*, *D*, *E*, and *O*, respectively. The distance of *OA*, *OB*, and *OC* are marked by solid red, blue, and brown lines following the same color scheme as in Fig. 2(d), respectively.

For the nonmagnetic hexagonal phase shown in Fig. 7(a), threefold symmetry is preserved; thus, $OA = OB = OC$. For both the orthorhombic and monoclinic phases of FeGe, they can be driven by either A_6^- or Γ_6^- lattice instabilities (Appendix G). Note that A_6^- and Γ_6^- lattice instabilities give rise to a similar unit-cell shape. The difference is that A_6^- leads to unit-cell doubling along the c axis while Γ_6^- does not. Since we focus on the $k_z = 0$ plane, the A_6^- and Γ_6^- lattice instabilities contribute to similar Bragg peak structures in momentum space.

In Fig. 7(b), we show the simulation of the orthorhombic phase in momentum space. Because of the in-plane unit-cell doubling [Fig. 1(c)], new Bragg peaks appear in either the OA, OB, or OC directions corresponding to different domain orientations. For illustration purposes, we show that new Bragg peaks appear in the OA direction, e.g., at half of OD and equivalent positions. The rectangular shape of the $OEBD$ restricts the diagonal of the rectangle to be equal, namely, $DE = OB$. Since $DE = OC$, we obtain $OB = OC$. Because of the threefold symmetry breaking, OB and OC deviate from OA. As a consequence, we obtain the relation $OB = OC \neq OA$.

For the monoclinic phase, the symmetry is lower than the orthorhombic phase. The restriction that $OB = OC$ is removed. Thus, we obtain $OB \neq OC \neq OA$.

APPENDIX D: STRUCTURE FACTOR ANALYSIS FOR THE (2 0 0) AND ITS EQUIVALENT BRAGG PEAKS

In the undistorted hexagonal phase, the Fe and Ge atoms all occupy the high-symmetry positions (Wyckoff position: $3f$ for Fe, $1a$ for Ge^1, and $2d$ for Ge^2). The neutron scattering structure factor for a general nuclear Bragg peak $\mathbf{Q}_{HKL} = (H, K, L)$ is given by

$$\begin{aligned} F_{\mathrm{hex}}(H,K,L) &= b_{\mathrm{Fe}}\Sigma_j^3 e^{i\mathbf{Q}_{HKL}\cdot\mathbf{R}(\mathrm{Fe}^j)} + b_{\mathrm{Ge}}\Sigma_j^3 e^{i\mathbf{Q}_{HKL}\cdot\mathbf{R}(\mathrm{Ge}^j)} \\ &= b_{\mathrm{Fe}}[e^{i2\pi(H/2)} + e^{i2\pi(K/2)} + e^{i2\pi(H/2+K/2)}] \\ &\quad + b_{\mathrm{Ge}}[e^{i2\pi(0)} + e^{i2\pi(H/3+2K/3+L/2)} + e^{i2\pi(2H/3+K/3+L/2)}]. \end{aligned}$$

Here, b_{Fe} and b_{Ge} are the neutron scattering lengths for the Fe and Ge nuclei, respectively, and $\mathbf{R}(\mathrm{Fe}^j)$ and $\mathbf{R}(\mathrm{Ge}^j)$ are the fractional coordinates for Fe and Ge, respectively. Note that j is the index for the three Fe and Ge atoms in one unit cell. For (2, 0, 0) and its equivalent Bragg peaks, the above formula results in the following:

$$F_{\mathrm{hex}}(2,0,0) = 3 \cdot b_{\mathrm{Fe}} + 0 \cdot b_{\mathrm{Ge}}.$$

It is clear that in the undistorted hexagonal phase, the (2, 0, 0) and its equivalent Bragg peaks only have a Fe contribution because the three Ge atoms in the unit cell add up destructively at this particular reciprocal space position while the three Fe atoms add up constructively.

The above equations for the structure factor still hold in the case of the slightly distorted lattice. The difference is that in the distorted lattice, the site symmetry for both Fe and Ge atoms will be lower compared with the hexagonal phase. Thus, the in-plane coordinates of Fe and Ge are no longer protected by the point-group symmetry of the hexagonal phase and can deviate from the high-symmetry fractional numbers of $\frac{1}{2}, \frac{1}{3}$, and $\frac{2}{3}$. In this case, the Ge contribution to the (2, 0, 0), (0, 2, 0), and $(2, -2, 0)$ Bragg peaks will not exactly cancel out. Since the lattice distortion obtained from the Larmor diffraction measurement is of the order of 10^{-4}, the Ge component at those Bragg positions should also be approximately 10^{-4} compared to the Fe component. Because the lattice spacing difference obtained in Larmor data is based on measurements of (2, 0, 0), (0, 2, 0), and $(2, -2, 0)$ Bragg peaks, these results are mainly affected by the Fe sublattice in the kagome plane.

APPENDIX E: GROUP-THEORETICAL ANALYSIS OF THE RAMAN-ACTIVE MODES OF THE NONMAGNETIC FeGe

In this appendix, we discuss the group-theoretical analysis of the phonon modes in the high-temperature nonmagnetic phase ($T > T_{\mathrm{N}}$). The high-temperature nonmagnetic FeGe belongs to the hexagonal structure with space group $P6/mmm$ (No. 191) (point group: D_{6h}). The Fe, Ge^1 (in the kagome layer), and Ge^2 atoms (in the honeycomb layer) have Wyckoff positions $3f$, $1a$, and $2d$, respectively. From the group theoretical considerations [71], Γ-point phonon modes of the hexagonal nonmagnetic FeGe can be expressed as $\Gamma_{\mathrm{total}} = 3A_{2u} \oplus B_{2g} \oplus B_{1u} \oplus B_{2u} \oplus E_{2u} \oplus E_{2g} \oplus 4E_{1u}$. Raman active modes are $\Gamma_{\mathrm{Raman}} = E_{2g}$, IR active modes are $\Gamma_{\mathrm{IR}} = 2A_{2u} \oplus 3E_{1u}$, the acoustic mode is $\Gamma_{\mathrm{acoustic}} = A_{2u} \oplus E_{1u}$, and the silent modes are $\Gamma_{\mathrm{silent}} = B_{2g} \oplus B_{1u} \oplus B_{2u} \oplus E_{2u}$. Note that (1) the Raman-active E_{2g} mode is related to the in-plane lattice vibrations of the Ge^2 atoms of the honeycomb layer; (2) E_{2g} and A_{1g} modes can be accessed from the ab-plane measurement while the E_{1g} mode can only be accessed from the side surface measurement; (3) the A_{1g} and E_{1g} modes are not symmetry allowed in the high-temperature nonmagnetic phase; and (4) there are no Raman-active modes for Fe and Ge^1 atoms in the kagome layer of the high-temperature nonmagnetic phase.

APPENDIX F: ROBUSTNESS OF THE A_6^- LATTICE INSTABILITY

In this appendix, we show that the A_6^- lattice instability is robust for a reasonable range of parameters in the DFT calculations.

TABLE II. Three lowest phonon modes at the A point based on the DFT phonon calculations at different ISMEAR and SIGMA parameters.

Smearing method	Smearing width (eV)	U (eV)	Magnetism?	Softest A point modes (cm^{-1})		
Gaussian	0.05	0	···	−172	105	210
Gaussian	0.20	0	···	−71	118	216
Fermi	0.05	0	···	−193	104	210
Fermi	0.10	0	···	−165	105	210
Fermi	0.20	0	···	−123	109	212
Fermi	0.20	1	···	−128	108	212
Fermi	0.20	2	···	−131	107	213
Fermi	0.20	3	···	−104	110	218
Fermi	0.20	0	AFM	78	168	248
Fermi	0.20	1	AFM	82	177	262
Fermi	0.20	2	AFM	87	184	277
Fermi	0.20	3	AFM	90	191	291

Two input parameters, which are not well determined but can affect the outcome of this type of first-principles calculation, are the Hubbard +U and the Fermi surface smearing parameter σ. The +U correction helps to capture the on-site repulsion between the d electrons for the transition metal, and the σ parameter determines how the partial occupancies near the Fermi level are treated. In systems where the lattice instabilities are intertwined and possibly driven by the Fermi surface effects, σ can lead to very large changes for the unstable mode frequencies. As a result, different values of σ should be examined to ensure the robustness of the reported unstable modes.

In Table II, we show the lowest three phonon frequencies at the A point with different σ values and smearing types (the "ISMEAR" tag in VASP, which determines Gaussian vs Fermi smearing). In the absence of a magnetic order, we always find an A_6^- instability. This calculation is performed in a $1 \times 1 \times 2$ supercell using the frozen-phonon approach in order to avoid the possible errors in the procedure used to obtain phonon dispersions. When the calculation is performed without spin polarization, there is a single A-point mode that is sensitive to the smearing width but is consistently unstable. When the magnetically ordered (AFM) phase is considered, this mode becomes stable. The absence of an A-point instability in the AFM phase is consistent with the DFT calculations shown in Refs. [42,45,48,49], and it suggests that the instability at the A point is very sensitive to the magnetic order.

One drawback for a DFT phonon calculation without taking the magnetic order into account is that fictitious instabilities may emerge throughout the Brillouin zone. While this is not the case for the phonon dispersions presented in Fig. 3(b), we performed frozen-phonon calculations in a $2 \times 2 \times 2$ supercell to confirm this observation and extract the representations of the instabilities. This supercell is commensurate with the Γ, M, L, and A points of the Brillouin zone. In Table III, we list the softest phonon frequencies on these points. There are no other instabilities at high-symmetry points other than those in Fig. 3(b).

TABLE III. Unstable phonon modes and their irreducible representations for the high-symmetry points in k space based on the DFT phonon calculation in a $2 \times 2 \times 2$ supercell. (No magnetic order was imposed, and $U = 2$ eV was used.)

Frequency (cm^{-1})	Degeneracy	Representation
98	3	L_2^-
71	2	Γ_5^-
63	1	A_3^-
35	3	L_3^-
21	3	M_2^+
0	2	Γ_6^-
0	1	Γ_2^-
$38i$	1	Γ_3^-
$45i$	3	M_3^-
$113i$	2	Γ_6^-
$132i$	2	A_6^-

APPENDIX G: GROUP-SUBGROUP ANALYSIS

In Tables IV and V, we show the low-symmetry space groups that can be obtained from the parent P6/mmm by the symmetry-breaking Γ_6^- and A_6^- irreducible representations (irreps).

The A_6^- instability can drive a transition to orthorhombic space groups Cmcm (#63, point group D_{2h}) or monoclinic $P2_1/m$ (#11, point group C_{2h}). The Γ_6^- instability, if it freezes in and drives the transition to a lower-symmetry phase, leads to either the orthorhombic space group Amm2 (point group C_{2v}) or the monoclinic space group Pm (point group C_s). The conclusion is the same: that both A_6^- and Γ_6^- lead to either the orthorhombic or monoclinic phase, breaking the threefold symmetry at T_N. The difference is

TABLE IV. Low-symmetry space groups that can be obtained from the parent P6/mmm by the symmetry-breaking A_6^- irrep.

Direction	Space group	Fe sites	Ge sites
A_6^- (a,0)	Cmcm (# 63)	4c, 8g	4c, 8f
A_6^- (0,a)	Cmcm (# 63)	4c, 8g	4c, 8e
A_6^- (a,b)	$P2_1/m$ (#11)	2e, 2e, 2e	2e, 4f

TABLE V. Low-symmetry space groups that can be obtained from the parent P6/mmm by the symmetry-breaking Γ_6^- irrep.

Direction	Space group	Fe sites	Ge sites
Γ_6^- (0,a)	Amm2 (# 38)	2a, 4d	2a, 2b, 2b
Γ_6^- (a,$\sqrt{3}$a)	Amm2 (# 38)	2a, 4d	2a, 4e
Γ_6^- (a,b)	Pm (#6)	1a, 1a, 1a	1a, 1b, 1b

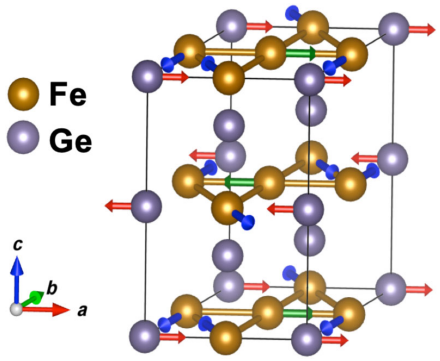

FIG. 8. The A_6^- displacement pattern of the nonmagnetic phase based on the DFT phonon calculation.

that A_6^- leads to a doubling of the unit cell along the c-axis direction while Γ_6^- does not. However, all of the low-symmetry structures have a large number of Raman-active modes, most of which are too weak to give rise to detectable mode intensity. Thus, a Γ_6^- lattice instability does not fundamentally change our conclusions, except that the interlayer c-axis dimerlike singlet cannot be formed due to the Γ_6^- mode.

APPENDIX H: A_6^- DISPLACEMENT

In this appendix, we present the A_6^- displacement pattern for the nonmagnetic hexagonal phase shown in Fig. 8 based on the DFT phonon calculations for the nonmagnetic phase.

APPENDIX I: RAMAN TENSOR ANALYSIS

The Raman tensor R_μ for an irreducible representation (μ) of a point group is a 2×2 matrix. With the unit vectors for the polarization of the incident light ($\hat{e}_i$) and scattering light ($\hat{e}_s$), the phononic Raman response is described in the following way:

$$\chi''_{\hat{e}_i\hat{e}_s} = \sum_\mu |\hat{e}_i R_\mu \hat{e}_s|^2. \tag{I1}$$

1. D_{6h} Raman tensor

The Raman tensors R_μ ($\mu = A_{1g}, A_{2g}, E_{1g}, E_{2g}$) for the irreducible representations (μ) of point group D_{6h} have the following forms:

$$\begin{pmatrix} a & 0 & 0 \\ 0 & a & 0 \\ 0 & 0 & b \end{pmatrix}, \begin{pmatrix} 0 & c & 0 \\ -c & 0 & 0 \\ 0 & 0 & 0 \end{pmatrix}, \begin{pmatrix} 0 & 0 & 0 \\ 0 & 0 & d \\ 0 & e & 0 \end{pmatrix} \begin{pmatrix} 0 & 0 & -d \\ 0 & 0 & 0 \\ -e & 0 & 0 \end{pmatrix},$$
$$\begin{pmatrix} 0 & f & 0 \\ f & 0 & 0 \\ 0 & 0 & 0 \end{pmatrix} \begin{pmatrix} f & 0 & 0 \\ 0 & -f & 0 \\ 0 & 0 & 0 \end{pmatrix}.$$

We choose $\hat{e}_i$ and $\hat{e}_s$ to be X, Y, R, and L, where $X = (100)$, $Y = (010)$, $R = 1/\sqrt{2}(1i0)$, and $L = 1/\sqrt{2}(1-i0)$.

Based on Eq. (I1), we obtain

$$\begin{aligned} \chi''^{D_{6h}}_{XX} &= a^2 + f^2, \\ \chi''^{D_{6h}}_{XY} &= c^2 + f^2, \\ \chi''^{D_{6h}}_{RR} &= a^2 + c^2, \\ \chi''^{D_{6h}}_{RL} &= 2f^2. \end{aligned} \tag{I2}$$

Thus, the Raman selection rules for the D_{6h} point group indicate that the XX, XY, RR, and RL polarization geometries probe the $A_{1g} + E_{2g}$, $A_{2g} + E_{2g}$, $A_{1g} + A_{2g}$, and $2E_{2g}$ symmetry excitations, respectively (Table VI).

The sum rule that $\chi''^{D_{6h}}_{XX} + \chi''^{D_{6h}}_{XY} = \chi''^{D_{6h}}_{RR} + \chi''^{D_{6h}}_{RL} = a^2 + c^2 + 2f^2$ sets a constraint for the Raman response in different scattering geometries, thus providing a unique way to check the data consistency.

From Eq. (I2), we can calculate the square of the Raman tensor element:

$$\begin{aligned} a^2 &= \chi''^{D_{6h}}_{XX} - \chi''^{D_{6h}}_{RL}/2, \\ c^2 &= \chi''^{D_{6h}}_{XY} - \chi''^{D_{6h}}_{RL}/2, \\ f^2 &= \chi''^{D_{6h}}_{RL}/2. \end{aligned} \tag{I3}$$

Therefore, the algebra in Eq. (I3) can be used to decompose the measured Raman signal into three separate irreducible representations (A_{1g}, A_{2g}, E_{2g}) of the point group D_{6h} (Table VII).

This decomposition algebra is a characteristic property of a lattice system with trigonal or hexagonal symmetry, where the threefold rotational symmetry is preserved.

TABLE VI. Relationship between the scattering geometries and the symmetry channels. Here, A_{1g}, A_{2g}, and E_{2g} are the irreducible representations of the D_{6h} point group.

Scattering geometry	Symmetry channel
XX	$A_{1g} + E_{2g}$
XY	$A_{2g} + E_{2g}$
RR	$A_{1g} + A_{2g}$
RL	$2E_{2g}$

TABLE VII. Algebra used to decompose the Raman data into three irreducible representations of the point group D_{6h}.

Symmetry channel	Expression
A_{1g}	$\chi''_{XX} - \chi''_{RL}/2$
A_{2g}	$\chi''_{XY} - \chi''_{RL}/2$
E_{2g}	$\chi''_{RL}/2$

Whether sixfold rotational symmetry is preserved or not depends on the system.

2. C_{2h} Raman tensor

The Raman tensors R_μ for the irreducible representation of point group C_{2h} ($\mu = A_g, B_g$) have the following form:

$$\begin{pmatrix} p & t & 0 \\ s & q & 0 \\ 0 & 0 & r \end{pmatrix}, \begin{pmatrix} 0 & 0 & w \\ 0 & 0 & r \\ u & v & 0 \end{pmatrix}.$$

For the A_6^--driven AFM monoclinic phase, the C_2 axis is perpendicular to the threefold axis of the nonmagnetic phase. In this case, we choose $\hat{e}_i$ and $\hat{e}_s$ to be X, Y, R, and L, where $X = (1\ \ 0\ \ 0)$, $Y = (0\ \ 0\ \ 1)$, $R = 1/\sqrt{2}(1\ \ 0\ \ i)$, and $L = 1/\sqrt{2}(1\ \ 0\ \ -i)$. Note that the choice of $\hat{e}_i$ and $\hat{e}_s$ is with respect to the monoclinic Raman tensor where the C_2 axis lies in the ab plane. Following Eq. (I1), we obtain

$$\begin{aligned} \chi''^{C_{2h}}_{XX} &= p^2, \\ \chi''^{C_{2h}}_{YY} &= r^2, \\ \chi''^{C_{2h}}_{XY} &= w^2, \\ \chi''^{C_{2h}}_{RR} &= 1/4((p+r)^2 + (u-w)^2), \\ \chi''^{C_{2h}}_{RL} &= 1/4((p-r)^2 + (u+w)^2). \end{aligned} \tag{I4}$$

The Raman selection rules for the C_{2h} point group in a single-domain sample indicate that XX, YY, and XY polarization geometries probe the A_g, A_g, and B_g symmetry excitations, respectively (Table VIII).

Since the monoclinic lattice distortion is about 3×10^{-4} at room temperature in the AFM phase [Fig. 2(g)], the anisotropy of the Raman tensor elements would be tiny. We thus obtain $p \sim r$ and $u \sim w$. According to Eq. (I4), RR mainly probes the A_g symmetry excitations while RL mainly probes the B_g symmetry excitations.

In the case of $p \sim r$ and $u \sim w$, the decomposition rule recovers to the D_{6h} case shown in Table VII. The two modes in between 160 and 162 cm^{-1} can be separated using the decomposition rules shown in Table VII. As we show in Fig. 9, a broader peak at around 160 cm^{-1} in the $XX - RL/2$ channel and a sharper mode at 162 cm^{-1} in the $RL/2$ channel can be clearly seen, while there is barely any phonon intensity in the $XY - RL/2$ channel. The application of the decomposition rule according to the point group D_{6h} for FeGe additionally confirms that the AFM monoclinic phase only slightly deviates from the hexagonal lattice.

TABLE VIII. Relationship between the scattering geometries and the symmetry channels for the C_{2h} Raman tensor. Here, A_g and B_g are the irreducible representations of the C_{2h} point group.

Scattering geometry	Symmetry channel
XX	A_g
YY	A_g
XY	B_g
RR	Mainly A_g
RL	Mainly B_g

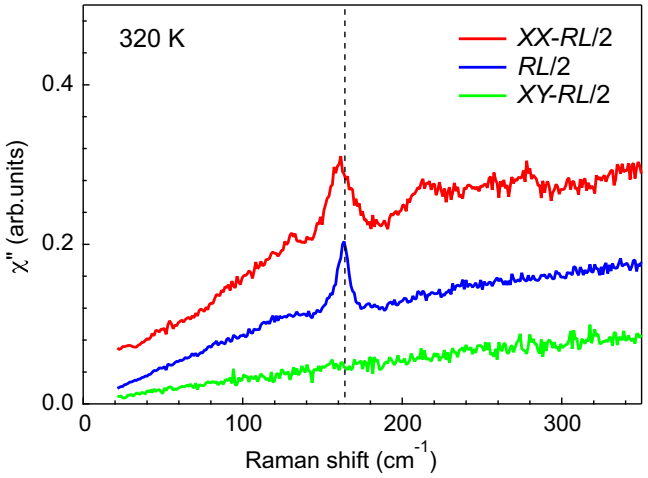

FIG. 9. Symmetry decompositions into separate channels using the decomposition rules shown in Table VII for FeGe at 320 K.

APPENDIX J: PHONON PEAK POSITIONS IN THE CDW PHASE

In this appendix, we present a summary of the phonon peak positions in the CDW phase at 90 K in Table IX.

TABLE IX. Experimentally observed phonon frequencies at the Brillouin zone center for FeGe in the CDW phase at 90 K. All the units are in cm^{-1}.

Scattering geometry	Frequency
RR	100
	127
	174
	203
	249
RL	84
	116
	130
	140
	166
	171
	233
	248
	265

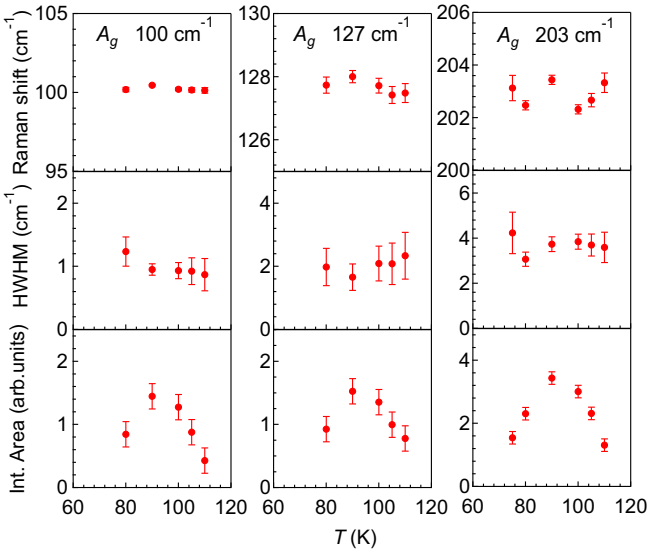

FIG. 10. The T dependence of the peak position, HWHM, and integrated intensity for the A_g phonon mode at 100 cm^{-1}, 127 cm^{-1}, and 203 cm^{-1} in the RR scattering geometry. The error bars represent 1 standard deviation.

APPENDIX K: FITTING PARAMETERS FOR THE A_g CDW MODES

In this appendix, we discuss the T dependence of the peak position, HWHM, and integrated intensity for the three A_g phonon modes at 100 cm^{-1}, 127 cm^{-1}, and 203 cm^{-1} in the RR scattering geometries below T_{CDW}. As shown in Fig. 10, the T dependence of the peak frequencies for the three modes does not change much between 60 K and 110 K. The HWHM for the three modes becomes a bit larger when approaching T_{canting}, similar to the A_g mode at 160 cm^{-1} shown in Fig. 5(c) of the main text. The integrated intensities for the three modes first increase below T_{CDW}, reach a maximum at 90 K, then decrease below 90 K, and finally become zero at T_{canting}. They are consistent with the T dependence for the A_g mode at 160 cm^{-1} shown in Fig. 5(c) of the main text.

APPENDIX L: COUPLED TWO-LORENTZIAN-PHONON MODEL

In this appendix, we present the fitting model for the peak at 162 cm^{-1} and the shoulder peak between T_{CDW} and T_{canting} in the RL scattering geometry.

Both the peak at 162 cm^{-1} and the shoulder peak on the lower-energy side have B_g symmetry; thus, they are allowed to be coupled. An interaction between the two modes can induce spectra weight transfer and also repelling of energy levels. We use Green's function formalism to construct a model describing the main mode (p_1) and its shoulder peak (p_2) [76].

The Raman response of the coupled modes can be calculated from an interacting Green's function:

$$\chi'' \sim \mathrm{Im} T^{\mathrm{T}} G T, \tag{L1}$$

where $T = [t_{p1}, t_{p2}]$, and t_{p1} and t_{p2} represent the light coupling amplitudes to the main peak p_1 and the shoulder peak p_2 in the RL scattering geometries, respectively. The superscript T denotes the transpose operation, and G is the Green's function for the two interacting phononic systems. The Green's function G can be obtained via the Dyson equation

$$G = (G_0^{-1} - V)^{-1}, \tag{L2}$$

where G_0 is the bare Green's function and V represents the interaction. Here, we consider two Lorentzian peaks that are coupled to each other.

The bare Green's function G_0 is

$$G_0 = \begin{pmatrix} G_{p1} & 0 \\ 0 & G_{p2} \end{pmatrix}, \tag{L3}$$

where G_{p1} and G_{p2} represent the bare main mode and the bare shoulder mode, respectively. They have the Lorentzian forms $G_{p1} = -1/(\omega - \omega_{p1} + i\gamma_{p1}) + 1/(\omega + \omega_{p1} + i\gamma_{p1})$ and $G_{p2} = -1/(\omega - \omega_{p2} + i\gamma_{p2}) + 1/(\omega + \omega_{p2} + i\gamma_{p2})$, where ω_{p1} and ω_{p2} are bare frequencies, and γ_{p_1} and γ_{p_2} are bare HWHMs.

Note that V is an off-diagonal matrix that describes the coupling strength v between the two modes:

$$V = \begin{pmatrix} 0 & v \\ v & 0 \end{pmatrix}. \tag{L4}$$

Inserting Eq. (L2)–(L4) into Eq. (L1), we obtain the coupled two-Lorentzian phonon model. By fitting the Raman data shown in Fig. 5(e), we obtain the bare mode energy, HWHM, and the light coupling amplitudes, as well as the integrated areas for the two bare modes between T_{CDW} and T_{canting} in the RL scattering geometry. The temperature dependence of these parameters is shown in Fig. 5(f) of the main text.

APPENDIX M: ANHARMONIC PHONON DECAY MODEL

In this appendix, we discuss the anharmonic phonon decay model. We fit the temperature dependence of the phonon frequency and HWHM using the anharmonic phonon decay model [80,81]:

$$\omega(T) = \omega_0 - C_1[1 + 2n(\Omega(T)/2)], \tag{M1}$$

$$\Gamma(T) = \gamma_0 + \gamma_1[1 + 2n(\Omega(T)/2)], \tag{M2}$$

where $\Omega(T) = \hbar\omega/k_B T$, $n(x) = 1/(e^x - 1)$ is the Bose-Einstein distribution function. Note that $\omega(T)$ and $\Gamma(T)$ involve mainly three-phonon decay processes, where an optical phonon decays into two acoustic modes with equal energy and opposite momentum.

[1] L. D. Landau, *On the theory of phase transitions. I*, Zh. Eksp. Teor. Fiz. **7**, 19 (1937).

[2] L. D. Landau and E. M. Lifshitz, *Statistical Physics* (Pergamon Press, New York, 1969), Vol. 5, Chap. 14.

[3] P. Toledano and J. Toledano, *Landau Theory of Phase Transitions: The Application to Structural, Incommensurate, Magnetic and Liquid Crystal Systems* (World Scientific Publishing Company, Singapore, 1987).

[4] Muzaffar Iqbal Khan and Trilok Chandra Upadhyay, *Phase transitions in H-bonded deuterated Rochelle salt crystal*, Eur. Phys. J. Plus **136**, 101 (2021).

[5] R. T. Harley, W. Hayes, A. M. Perry, S. R. P. Smith, R. J. Elliott, and I. D. Saville, *Cooperative Jahn-Teller effects in the mixed crystals* $Tb_pGd_{1-p}VO_4$ *and* $Dy_pY_{1-p}VO_4$, J. Phys. C **7**, 3145 (1974).

[6] J. D. Axe, A. H. Moudden, D. Hohlwein, D. E. Cox, K. M. Mohanty, A. R. Moodenbaugh, and Youwen Xu, *Structural phase transformations and superconductivity in* $La_{2-x}Ba_xCuO_4$, Phys. Rev. Lett. **62**, 2751 (1989).

[7] S. Avci, O. Chmaissem, J. M. Allred, S. Rosenkranz, I. Eremin, A. V. Chubukov, D. E. Bugaris, D. Y. Chung, M. G. Kanatzidis, J.-P. Castellan, J. A. Schlueter, H. Claus, D. D. Khalyavin, P. Manuel, A. Daoud-Aladine, and R. Osborn, *Magnetically driven suppression of nematic order in an iron-based superconductor*, Nat. Commun. **5**, 3845 (2014).

[8] L. Wang, F. Hardy, A. E. Böhmer, T. Wolf, P. Schweiss, and C. Meingast, *Complex phase diagram of* $Ba_{1-x}Na_xFe_2As_2$*: A multitude of phases striving for the electronic entropy*, Phys. Rev. B **93**, 014514 (2016).

[9] Jeremiah P. Tidey, Christopher Keegan, Nicholas C. Bristowe, Arash A. Mostofi, Zih-Mei Hong, Bo-Hao Chen, Yu-Chun Chuang, Wei-Tin Chen, and Mark S. Senn, *Structural origins of the low-temperature orthorhombic to low-temperature tetragonal phase transition in high-*T_c *cuprates*, Phys. Rev. B **106**, 085112 (2022).

[10] Pengcheng Dai, *Antiferromagnetic order and spin dynamics in iron-based superconductors*, Rev. Mod. Phys. **87**, 855 (2015).

[11] A. E. Böhmer, F. Hardy, L. Wang, T. Wolf, P. Schweiss, and C. Meingast, *Superconductivity-induced re-entrance of the orthorhombic distortion in* $Ba_{1x}K_xFe_2As_2$, Nat. Commun. **6**, 7911 (2015).

[12] J. M. Allred, K. M. Taddei, D. E. Bugaris, M. J. Krogstad, S. H. Lapidus, D. Y. Chung, H. Claus, M. G. Kanatzidis, D. E. Brown, J. Kang, R. M. Fernandes, I. Eremin, S. Rosenkranz, O. Chmaissem, and R. Osborn, *Double-Q spin-density wave in iron arsenide superconductors*, Nat. Phys. **12**, 493 (2016).

[13] Morten H. Christensen, Peter P. Orth, Brian M. Andersen, and Rafael M. Fernandes, *Emergent magnetic degeneracy in iron pnictides due to the interplay between spin-orbit coupling and quantum fluctuations*, Phys. Rev. Lett. **121**, 057001 (2018).

[14] Morten H. Christensen, Peter P. Orth, Brian M. Andersen, and Rafael M. Fernandes, *Magnetic phase diagram of the iron pnictides in the presence of spin-orbit coupling: Frustration between* C_2 *and* C_4 *magnetic phases*, Phys. Rev. B **98**, 014523 (2018).

[15] Itiro Syôzi, *Statistics of kagome lattice*, Prog. Theor. Phys. **6**, 306 (1951).

[16] C. Broholm, R. J. Cava, S. A. Kivelson, D. G. Nocera, M. R. Norman, and T. Senthil, *Quantum spin liquids*, Science **367**, eaay0668 (2020).

[17] Wan-Sheng Wang, Zheng-Zhao Li, Yuan-Yuan Xiang, and Qiang-Hua Wang, *Competing electronic orders on kagome lattices at van Hove filling*, Phys. Rev. B **87**, 115135 (2013).

[18] Maximilian L. Kiesel, Christian Platt, and Ronny Thomale, *Unconventional Fermi surface instabilities in the kagome Hubbard model*, Phys. Rev. Lett. **110**, 126405 (2013).

[19] Brenden R. Ortiz, Lídia C. Gomes, Jennifer R. Morey, Michal Winiarski, Mitchell Bordelon, John S. Mangum, Iain W. H. Oswald, Jose A. Rodriguez-Rivera, James R. Neilson, Stephen D. Wilson, Elif Ertekin, Tyrel M. McQueen, and Eric S. Toberer, *New kagome prototype materials: Discovery of* KV_3Sb_5, RbV_3Sb_5, *and* CsV_3Sb_5, Phys. Rev. Mater. **3**, 094407 (2019).

[20] Xilin Feng, Kun Jiang, Ziqiang Wang, and Jiangping Hu, *Chiral flux phase in the Kagome superconductor* AV_3Sb_5, Sci. Bull. **66**, 1384 (2021).

[21] Yu-Xiao Jiang *et al.*, *Unconventional chiral charge order in kagome superconductor* KV_3Sb_5, Nat. Mater. **20**, 1353 (2021).

[22] M. Michael Denner, Ronny Thomale, and Titus Neupert, *Analysis of charge order in the kagome metal* AV_3Sb_5 *(*$A = $ K, Rb, Cs*)*, Phys. Rev. Lett. **127**, 217601 (2021).

[23] Takamori Park, Mengxing Ye, and Leon Balents, *Electronic instabilities of kagome metals: Saddle points and Landau theory*, Phys. Rev. B **104**, 035142 (2021).

[24] Rina Tazai, Youichi Yamakawa, Seiichiro Onari, and Hiroshi Kontani, *Mechanism of exotic density-wave and beyond-Migdal unconventional superconductivity in kagome metal* AV_3Sb_5 *(*A = K*, Rb, Cs)*, Sci. Adv. **8**, eabl4108 (2022).

[25] Yaofeng Xie, Yongkai Li, Philippe Bourges, Alexandre Ivanov, Zijin Ye, Jia-Xin Yin, M. Zahid Hasan, Aiyun Luo, Yugui Yao, Zhiwei Wang, Gang Xu, and Pengcheng Dai, *Electron-phonon coupling in the charge density wave state of* CsV_3Sb_5, Phys. Rev. B **105**, L140501 (2022).

[26] Hui Chen *et al.*, *Roton pair density wave in a strong-coupling kagome superconductor*, Nature (London) **599**, 222 (2021).

[27] Kun Jiang, Tao Wu, Jia-Xin Yin, Zhenyu Wang, M. Zahid Hasan, Stephen D. Wilson, Xianhui Chen, and Jiangping Hu, *Kagome superconductors* AV_3Sb_5 *(*A = K, Rb, Cs*)*, Natl. Sci. Rev. **10**, nwac199 (2022).

[28] C. Mielke, D. Das, J.-X. Yin, H. Liu, R. Gupta, Y.-X. Jiang, M. Medarde, X. Wu, H. C. Lei, J. Chang, Pengcheng Dai, Q. Si, H. Miao, R. Thomale, T. Neupert, Y. Shi, R. Khasanov, M. Z. Hasan, H. Luetkens, and Z. Guguchia, *Time-reversal symmetry-breaking charge order in a kagome superconductor*, Nature (London) **602**, 245 (2022).

[29] Jia-Xin Yin, Biao Lian, and M. Zahid Hasan, *Topological kagome magnets and superconductors*, Nature (London) **612**, 647 (2022).

[30] Ying Xiang, Qing Li, Yongkai Li, Wei Xie, Huan Yang, Zhiwei Wang, Yugui Yao, and Hai-Hu Wen, *Twofold symmetry of c-axis resistivity in topological kagome superconductor* CsV_3Sb_5 *with in-plane rotating magnetic field*, Nat. Commun. **12**, 6727 (2021).

[31] He Zhao, Hong Li, Brenden R. Ortiz, Samuel M. L. Teicher, Takamori Park, Mengxing Ye, Ziqiang Wang, Leon Balents, Stephen D. Wilson, and Ilija Zeljkovic, *Cascade of correlated electron states in the kagome superconductor* CsV_3Sb_5, Nature (London) **599**, 216 (2021).

[32] Qiong Wu, Z. X. Wang, Q. M. Liu, R. S. Li, S. X. Xu, Q. W. Yin, C. S. Gong, Z. J. Tu, H. C. Lei, T. Dong, and N. L. Wang, *Simultaneous formation of two-fold rotation symmetry with charge order in the kagome superconductor* CsV_3Sb_5 *by optical polarization rotation measurement*, Phys. Rev. B **106**, 205109 (2022).

[33] Yishuai Xu, Zhuoliang Ni, Yizhou Liu, Brenden R. Ortiz, Qinwen Deng, Stephen D. Wilson, Binghai Yan, Leon Balents, and Liang Wu, *Three-state nematicity and magneto-optical Kerr effect in the charge density waves in kagome superconductors*, Nat. Phys. **18**, 1470 (2022).

[34] Linus Kautzsch, Brenden R. Ortiz, Krishnanand Mallayya, Jayden Plumb, Ganesh Pokharel, Jacob P. C. Ruff, Zahirul Islam, Eun-Ah Kim, Ram Seshadri, and Stephen D. Wilson, *Structural evolution of the kagome superconductors* AV_3Sb_5 *(*A = K, Rb, and Cs*) through charge density wave order*, Phys. Rev. Mater. **7**, 024806 (2023).

[35] Tetuo Ohoyama, Kazuo Kanematsu, and Kō Yasukōchi, *A new intermetallic compound* FeGe, J. Phys. Soc. Jpn. **18**, 589 (1963).

[36] O Beckman, K Carrander, L Lundgren, and M Richardson, *Susceptibility measurements and magnetic ordering of hexagonal* FeGe, Phys. Scr. **6**, 151 (1972).

[37] J. B. Forsyth, C. Wilkinson, and P. Gardner, *The low-temperature magnetic structure of hexagonal* FeGe, J. Phys. F **8**, 2195 (1978).

[38] J. Bernhard, B. Lebech, and O. Beckman, *Neutron diffraction studies of the low-temperature magnetic structure of hexagonal* FeGe, J. Phys. F **14**, 2379 (1984).

[39] Xiaokun Teng *et al.*, *Discovery of charge density wave in a kagome lattice antiferromagnet*, Nature (London) **609**, 490 (2022).

[40] Jia-Xin Yin *et al.*, *Discovery of charge order and corresponding edge state in kagome magnet* FeGe, Phys. Rev. Lett. **129**, 166401 (2022).

[41] Xiaokun Teng, Ji Seop Oh, Hengxin Tan, Lebing Chen, Jianwei Huang, Bin Gao, Jia-Xin Yin, Jiun-Haw Chu, Makoto Hashimoto, Donghui Lu, Chris Jozwiak, Aaron Bostwick, Eli Rotenberg, Garrett E. Granroth, Binghai Yan, Robert J. Birgeneau, Pengcheng Dai, and Ming Yi, *Magnetism and charge density wave order in kagome* FeGe, Nat. Phys. **19**, 814 (2023).

[42] H. Miao, T. T. Zhang, H. X. Li, G. Fabbris, A. H. Said, R. Tartaglia, T. Yilmaz, E. Vescovo, J.-X. Yin, S. Murakami, X. L. Feng, K. Jiang, X. L. Wu, A. F. Wang, S. Okamoto, Y. L. Wang, and H. N. Lee, *Signature of spin-phonon coupling driven charge density wave in a kagome magnet*, Nat. Commun. **14**, 6183 (2023).

[43] Ziyuan Chen, Xueliang Wu, Shiming Zhou, Jiakang Zhang, Ruotong Yin, Yuanji Li, Mingzhe Li, Jiashuo Gong, Mingquan He, Yisheng Chai, Xiaoyuan Zhou, Yilin Wang, Aifeng Wang, Ya-Jun Yan, and Dong-Lai Feng, *Long-ranged charge order conspired by magnetism and lattice in an antiferromagnetic Kagome metal*, arXiv:2307.07990.

[44] Chenfei Shi *et al.*, *Disordered structure for long-range charge density wave order in annealed crystals of magnetic kagome* FeGe, arXiv:2308.09034.

[45] Sen Shao, Jia-Xin Yin, Ilya Belopolski, Jing-Yang You, Tao Hou, Hongyu Chen, Yuxiao Jiang, Md Shafayat Hossain, Mohammad Yahyavi, Chia-Hsiu Hsu, Yuan Ping Feng, Arun Bansil, M. Zahid Hasan, and Guoqing Chang, *Intertwining of magnetism and charge ordering in kagome* FeGe, ACS Nano **17**, 10164 (2023).

[46] Hanjing Zhou, Songsong Yan, Dongze Fan, Di Wang, and Xiangang Wan, *Magnetic interactions and possible structural distortion in kagome* FeGe *from first-principles calculations and symmetry analysis*, Phys. Rev. B **108**, 035138 (2023).

[47] Chandan Setty, Christopher A. Lane, Lei Chen, Haoyu Hu, Jian-Xin Zhu, and Qimiao Si, *Electron correlations and charge density wave in the topological kagome metal* FeGe, arXiv:2203.01930.

[48] Hai-Yang Ma, Jia-Xin Yin, M. Zahid Hasan, and Jianpeng Liu, *Theory for charge density wave and orbital-flux state in antiferromagnetic kagome metal* FeGe, arXiv:2303.02824.

[49] Yilin Wang, *Enhanced spin-polarization via partial* Ge-*dimerization as the driving force of the charge density wave in* FeGe, Phys. Rev. Mater. **7**, 104006 (2023).

[50] Xingye Lu, Kuo-Feng Tseng, T. Keller, Wenliang Zhang, Ding Hu, Yu Song, Haoran Man, J. T. Park, Huiqian Luo, Shiliang Li, Andriy H. Nevidomskyy, and Pengcheng Dai, *Impact of uniaxial pressure on structural and magnetic phase transitions in electron-doped iron pnictides*, Phys. Rev. B **93**, 134519 (2016).

[51] F. Li, S. R. Parnell, W. A. Hamilton, B. B. Maranville, T. Wang, R. Semerad, D. V. Baxter, J. T. Cremer, and R. Pynn, *Superconducting magnetic Wollaston prism for neutron spin encoding*, Rev. Sci. Instrum. **85**, 053303 (2014).

[52] Weiyi Wang, Yu Song, Chongde Cao, Kuo-Feng Tseng, Thomas Keller, Yu Li, L. W. Harriger, Wei Tian, Songxue Chi, Rong Yu, Andriy H. Nevidomskyy, and Pengcheng Dai, *Local orthorhombic lattice distortions in the paramagnetic tetragonal phase of superconducting* $NaFe_{1-x}Ni_xAs$, Nat. Commun. **9**, 3128 (2018).

[53] B. Náfrádi, T. Keller, F. Hardy, C. Meingast, A. Erb, and B. Keimer, *Magnetostriction and magnetostructural domains in antiferromagnetic* $YBa_2Cu_3O_6$, Phys. Rev. Lett. **116**, 047001 (2016).

[54] T. P. Devereaux and R. Hackl, *Inelastic light scattering from correlated electrons*, Rev. Mod. Phys. **79**, 175 (2007).

[55] M. V. Klein, *Theory of Raman scattering from charge-density-wave phonons*, Phys. Rev. B **25**, 7192 (1982).

[56] John A. Holy, Miles V. Klein, W. L. McMillan, and S. F. Meyer, *Raman-active lattice vibrations of the*

commensurate superlattice in $2H-TaSe_2$, Phys. Rev. Lett. **37**, 1145 (1976).

[57] N. Nagaosa and E. Hanamura, *Microscopic theory on the Raman spectra of transition metal dichalcogenides in CDW state*, Solid State Commun. **41**, 809 (1982).

[58] Shangfei Wu, Brenden R. Ortiz, Hengxin Tan, Stephen D. Wilson, Binghai Yan, Turan Birol, and Girsh Blumberg, *Charge density wave order in the kagome metal* AV_3Sb_5 *(*A = Cs, Rb, K*)*, Phys. Rev. B **105**, 155106 (2022).

[59] Lebing Chen, Xiaokun Teng, Hengxin Tan, Barry L. Winn, Garrett E. Granorth, Feng Ye, D. H. Yu, R. A. Mole, Bin Gao, Binghai Yan, Ming Yi, and Pengcheng Dai, *Competing itinerant and local spin interactions in kagome metal* FeGe, Nat. Commun. **15**, 1918 (2024).

[60] R. E. Peierls, *Quantum Theory of Solids* (Oxford University Press, New York, 1955), p. 108.

[61] L. N. Bulaevskii, A. I. Buzdin, and D. I. Khomskii, *Spin-Peierls transition in magnetic field*, Solid State Commun. **27**, 5 (1978).

[62] James W. Bray, Leonard V. Interrante, Israel S. Jacobs, and Jill C. Bonner, "*The Spin-Peierls Transition*," in *Extended Linear Chain Compounds: Volume 3*, edited by Joel S. Miller (Springer, Boston, MA, 1983), pp. 353–415.

[63] W.-L. Zhang, Athena S. Sefat, H. Ding, P. Richard, and G. Blumberg, *Stress-induced nematicity in* $EuFe_2As_2$ *studied by Raman spectroscopy*, Phys. Rev. B **94**, 014513 (2016).

[64] L. Chauvière, Y. Gallais, M. Cazayous, A. Sacuto, M. A. Méasson, D. Colson, and A. Forget, *Doping dependence of the lattice dynamics in* $Ba(Fe_{1-x}Co_x)_2As_2$ *studied by Raman spectroscopy*, Phys. Rev. B **80**, 094504 (2009).

[65] William R. Meier, Qing-Ping Ding, Andreas Kreyssig, Sergey L. Bud'ko, Aashish Sapkota, Karunakar Kothapalli, Vladislav Borisov, Roser Valentí, Cristian D. Batista, Peter P. Orth, Rafael M. Fernandes, Alan I. Goldman, Yuji Furukawa, Anna E. Böhmer, and Paul C. Canfield, *Hedgehog spin-vortex crystal stabilized in a hole-doped iron-based superconductor*, npj Quantum Mater. **3**, 5 (2018).

[66] Xueliang Wu, Xinrun Mi, Long Zhang, Xiaoyuan Zhou, Mingquan He, Yisheng Chai, and Aifeng Wang, *Annealing tunable charge density wave order in a magnetic kagome material* FeGe, arXiv:2308.01291.

[67] John P. Perdew, Kieron Burke, and Matthias Ernzerhof, *Generalized gradient approximation made simple*, Phys. Rev. Lett. **77**, 3865 (1996).

[68] G. Kresse and J. Furthmüller, *Efficient iterative schemes for ab initio total-energy calculations using a plane-wave basis set*, Phys. Rev. B **54**, 11169 (1996).

[69] G. Kresse and J. Furthmller, *Efficiency of ab-initio total energy calculations for metals and semiconductors using a plane-wave basis set*, Comput. Mater. Sci. **6**, 15 (1996).

[70] Atsushi Togo and Isao Tanaka, *First principles phonon calculations in materials science*, Scr. Mater. **108**, 1 (2015).

[71] E. Kroumova, M. I. Aroyo, J. M. Perez-Mato, A. Kirov, C. Capillas, S. Ivantchev, and H. Wondratschek, *Bilbao crystallographic server: Useful databases and tools for phase-transition studies*, Phase Transit. **76**, 155 (2003).

[72] M. I. Aroyo, J. M. Perez-Mato, D. Orobengoa, E. Tasci, G. De La Flor, and A. Kirov, *Crystallography online: Bilbao crystallographic server*, Bulg Chem Commun **43**, 183 (2011), http://www.bcc.bas.bg/BCC_Volumes/Volume_43_Number_2_2011/Volume_43_Number_2_2011_PDF/BGG_2011_43_2.pdf.

[73] Dorian M. Hatch and Harold T. Stokes, *Invariants: Program for obtaining a list of invariant polynomials of the order-parameter components associated with irreducible representations of a space group*, J. Appl. Crystallogr. **36**, 951 (2003).

[74] A. P. Cracknell, B. L. Davies, S. C. Miller, and W. F. Love, *Kronecker Product Tables, General Introduction and Tables of Irreducible Representations of Space Groups* (IFI/Plenum, New York, 1979), Vol. 1.

[75] A. A. Maksimov, A. V. Puchkov, I. I. Tartakovskii, V. B. Timofeev, D. Reznik, and M. V. Klein, *Investigations of the temperature dependence of the low energy electronic Raman scattering in* $Ti_2Ba_2CaCu_2O_8$ *single crystals*, Solid State Commun. **81**, 407 (1992).

[76] Mai Ye, Xianghan Xu, Xiangyue Wang, Jaewook Kim, Sang-Wook Cheong, and Girsh Blumberg, *Crystal-field excitations and vibronic modes in the triangular-lattice spin-liquid candidate* $TbInO_3$, Phys. Rev. B **104**, 085102 (2021).

[77] H. M. Rosenberg, *The Solid State: An Introduction to the Physics of Crystals for Students of Physics, Materials Science, and Engineering* (Oxford University Press, Oxford, New York, 1988).

[78] H. T. Stokes, D. M. Hatch, and B. J. Campbell, *ISODISTORT, ISOTROPY Software Suite*, iso.byu.edu.

[79] Branton J. Campbell, Harold T. Stokes, David E. Tanner, and Dorian M. Hatch, *ISODISPLACE: A web-based tool for exploring structural distortions*, J. Appl. Crystallogr. **39**, 607 (2006).

[80] P. G. Klemens, *Anharmonic decay of optical phonons*, Phys. Rev. **148**, 845 (1966).

[81] José Menéndez and Manuel Cardona, *Temperature dependence of the first-order Raman scattering by phonons in* Si, Ge*, and* $\alpha-$Sn*: Anharmonic effects*, Phys. Rev. B **29**, 2051 (1984).